Review

Ferroelectric and Non-Linear Optical Nanofibers by Electrospinning: From Inorganics to Molecular Crystals

Rosa M. F. Baptista *, Etelvina de Matos Gomes, Michael Belsley, Bernardo Almeida *

Posted Date: 29 January 2025

doi: 10.20944/preprints202501.2184.v1

Keywords: piezoelectric ceramics; molecular crystals; electrospinning; nanofibers and microfibers; ferroelectrics; multiferroics; pyroelectricity; piezoelectricity; nonlinear optics; hybrid functional materials; energy harvesting

Review

Ferroelectric and Non-Linear Optical Nanofibers by Electrospinning: From Inorganics to Molecular Crystals

Rosa M. F. Baptista [1], * Etelvina de Matos Gomes [1], Michael Belsley [1] and Bernardo Almeida [1,*]

Centre of Physics of Minho and Porto Universities (CF-UM-UP), Laboratory of Physics for Materials and Emergent Technologies (LaPMET), University of Minho, Campus de Gualtar, 4710-057 Braga, Portugal

* Correspondence: rosa_batista@fisica.uminho.pt

Abstract: In recent decades, substantial progress has been made in embedding molecules, nanocrystals, and nanograins into nanofibers, resulting in a new class of hybrid functional materials with exceptional physical properties. Among these materials, functional nanofibers exhibiting ferroelectric, piezoelectric, pyroelectric, multiferroic, and nonlinear optical characteristics, have attracted considerable attention and undergone substantial improvements. This review critically examines these developments, focusing on strategies for incorporating diverse compounds into nanofibers and their impact on enhancing their physical properties, particularly ferroelectric behavior and nonlinear optical conversion. These developments have transformative potential across electronics, photonics, biomaterials, and energy harvesting. By synthesizing recent advancements in the design and application of nano-fiber embedded materials, this review seeks to highlight their potential impact on both scientific research, technological innovation and the development of next-generation devices.

Keywords: piezoelectric ceramics; molecular crystals; electrospinning; nanofibers and microfibers; ferroelectrics; multiferroics; pyroelectricity; piezoelectricity; nonlinear optics; hybrid functional materials; energy harvesting

1. Introduction

Nanofibers have emerged as a promising platform for advancing optical and electrical applications due to their unique structural and functional properties. Traditional piezoelectric ceramics, such as lead zirconate titanate (PZT), zinc oxide (ZnO), and barium titanate ($BaTiO_3$), exhibit remarkable piezoelectric performance. However, their inherent brittleness and the need for high processing temperatures (T > 600°C) significantly constrain their practical utility [1]. These limitations have driven the search for novel ferroelectric materials that are both flexible and more easily processed. Among these alternatives, ferroelectric fiber composites fabricated by electrospinning hold significant promise. These materials not only exhibit enhanced ferroelectric, piezoelectric, pyroelectric and non-linear optical (NLO) properties, but are also flexible, biocompatible and environmentally friendly.

Ferroelectricity is a characteristic of crystals with spontaneous polarization, which can alternate between two or more equivalent orientational states under an external electric field. These materials, belonging to a subset of pyroelectric crystals, inherently exhibit piezoelectricity [2]. Importantly, many practical applications of ferroelectric materials leverage their related properties, such as pyroelectricity and piezoelectricity, rather than ferroelectricity itself. For instance, pyroelectric materials find utility in imaging and detection applications [3,4], while piezoelectric materials are widely used in electromechanical devices. Notably, the high piezoelectric coefficients of materials such as PZT have enabled advancements in microelectromechanical systems (MEMS) and energy

 doi:10.20944/preprints202501.2184.v1

harvesting devices, including their miniaturization [3,5–8]. Ferroelectric materials are also widely used in capacitors for microelectronics, non-volatile memories, and sensors [9–12].

A key advantage of reducing ferroelectric materials to nanoscale dimensions is the substantial decrease in voltage required to achieve coercive fields, making them highly attractive for integration into modern electronic systems. For example, nanoscale ferroelectric structures require potential differences as low as 5 V to achieve coercive fields, compared to several kV in bulk crystals or ceramics [9].

Nanostructures with reduced dimensions, in the form of fibers, wires, rods, belts, tubes, and rings, have attracted significant interest for their unique properties and potential applications in sensing, flexible electronics, and nanoscale electrical energy generation. Among these, ferroelectric nanofibers offer unique advantages, as they do not require substrates and enable new functionalities. While several fabrications methods, including chemical vapor deposition (CVD) [13,14], hydrothermal methods [15], solid state reactions [16,17] and sol-gel [18–20] have been used to create nanostructures, these methods often involve complex procedures, expensive equipment, or costly precursor materials.

In contrast, electrospinning is a simple, versatile and cost-effective technique capable of producing continuous, individual fibers with a variety of structures, including inclusions, core-shell and 3D architectures [21–25]. Electrospinning enables the fabrications of nanofibers with diameters ranging from a few micrometers to less than 100 nm. Electrospinning stands out as a straightforward and adaptable technique capable of creating nanofibers from a wide range of polymers, often incorporating organic or semi-organic nanocrystals to create hybrid composite materials. This method has also been used to align nonlinear optical (NLO) chromophores in subwavelength structures with tailored functionalities [26].

Low-dimensional nanostructures, specifically ferroelectric nanofibers, have been successfully fabricated using the versatile electrospinning technique [27–32]. These nanofibers exhibit exceptional ferroelectric properties at the nanoscale making them highly promising for applications ranging from flexible electronic devices and highly sensitive sensors to nanogenerators for power generation. Additionally, electrospinning facilitates the integrations of multiple functionalities such as combining ferroelectric and magnetic properties within a single nanostructured entity. The demand for cost-effective sensors, actuators, and electronic components, coupled with the need for increased device integration, has spurred interest in exploring nanofibers with high aspect ratios and multifunctionality. Electrospun nanofibers offer an optimal solution, combining affordability, flexibility, and versatility.

Although recent studies have reviewed ferroelectric composites [11,33–38], there remains a notable gap in the literature concerning electrospun single-phase inorganic ferroelectric nanofibers and organic ferroelectric nanofibers beyond polyvinylidene fluoride (PVDF). While the synthesis and applications of nanofibers have been extensively studied, their ferroelectric and nonlinear optical properties are often overlooked. This review aims to address this gap by focusing on the ferroelectric and nonlinear optical characteristics of electrospun nanofibers, emphasizing the unique features and potential applications of both inorganic and organic ferroelectrics.

2. Electrospinning Process and Parameters

2.1. Electrospinning

Electrospinning is a widely used technique for synthesizing nanofibers based on the stretching of a viscoelastic solution and its consequent solidification under the influence of a strong electric field. Figure 1a illustrates schematic of a typical electrospinning system used for producing fiber mats. In this method, a high DC electric field (100 – 500 kV/m) is applied to a metallic capillary containing a polymer or sol-gel precursor solution. At the tip of the capillary, an electrically charged drop forms, with electric charges evenly distributed across its surface (Figure 1b).

 doi:10.20944/preprints202501.2184.v1

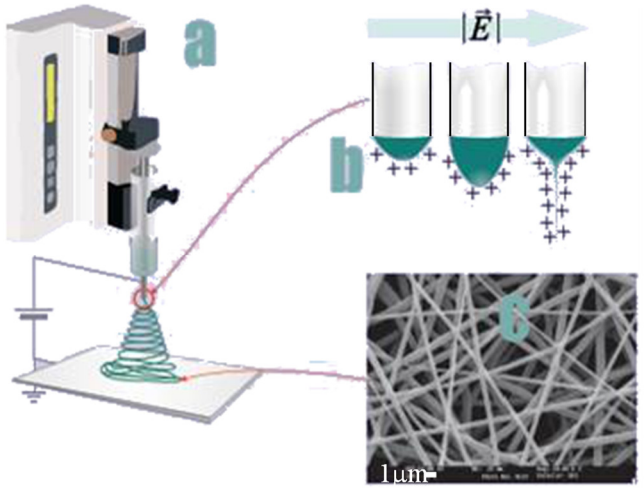

Figure 1. Electrospinning process, with a) typical experimental setup, b) Taylor cone formation and c) resulting fibers.

The interplay between the externally applied electric field, repulsive forces among surface charges, and the surface tension of the droplet induces a characteristic cone-shaped deformation known as the **Taylor cone**, typically exhibiting an angle of approximately 30° at its tip [22]. When the applied electric field exceeds a critical threshold, the electrostatic forces overcome the surface tension, leading to the ejection of a fine jet from the tip of the Taylor cone. The critical potential difference V_c required for jet emission for the emission of the jet takes place, assuming a spherical shape of the droplet at the cone's apex, is given by [25]:

$$V_c^2 = 0.36\left(\frac{D}{L}\right)^2\left(ln\left(\frac{2L}{R}\right)-\frac{3}{2}\right)(1.3\pi R\gamma) \quad , V_C \; in \; kV \tag{1}$$

where R is the radius of the syringe needle, L its length, D the distance between the needle and the collector and γ the surface tension of the solution. With the numerical factors V_C is expressed in kV.

Once the jet is emitted, it undergoes stretching due to the applied electric field, accompanied by instabilities arising from charge interactions. These instabilities result in the elongation and thinning of the jet, reducing its diameter as the solvent evaporates. In this way fibers are obtained that can reach, diameters down to a few tens of nanometers and lengths of several tens of meters (Figure 1c), in a controlled manner.

By tailoring the composition of the precursor solutions, it is possible to incorporate functional materials, such as ferroelectric or magnetic nanoparticles, into the fibers. This enables the creation of **functionalized composite nanofibers** with tunable properties for targeted applications. The high surface-to-volume ratio and aspect ratio (length-to-diameter) of the resulting fibers make electrospinning a versatile and powerful technique for fabricating micro- and nanoscale fibers with specific functionalities.

The final fiber diameter (d_f) is determined by the balance between surface tension and the repulsion of surface charges in the stretched jet. At the point where the jet ceases to thin further, the fiber diameter can be expressed as [25]:

$$d_f = \left(\gamma\varepsilon'\left(\frac{Q}{I}\right)^2\frac{2}{\pi(ln(\chi)-3)}\right)^{1/3} \tag{2}$$

where Q is the flow rate of the fluid jet, I is the electric current, ε′ is the permittivity of the environment (air), γ is the surface tension and χ is the dimensionless wavelength of the jet's torsional instability (proportional to the curvature radius of the bending perturbation divided by the jet radius). Consequently, the fiber diameter depends not only on the physical properties of the precursor

 doi:10.20944/preprints202501.2184.v1

solution (e.g., concentration, viscosity, conductivity) but also on process parameters such as the applied electric field, flow rate, and collection distance. Fiber diameter uniformity can be monitored by observing the stability of the electric current during the process. Any fluctuations in current often indicate variations in jet stability.

2.2. Process Parameters

The properties of the precursor solution and the corresponding processing parameters significantly influence the morphology and characteristics of the electrospun fibers. Key factors include polymer concentration, solvent properties, applied voltage, needle-to-collector distance, flow rate, and environmental conditions.

As polymer concentration or viscosity increases, the average fiber diameter tends to grow. This occurs because the higher viscosity resists elongation, slowing the jet's thinning process. Conversely, low-viscosity solutions often result in thinner fibers or, if the concentration is too low, the formation of droplets instead of continuous fibers (a phenomenon known as electrospraying).

Solvents with low vapor pressure typically produce thinner fibers. This is because slower solvent evaporation prolongs the jet's elongation and diameter reduction phases before solidification occurs. The choice of solvent also influences the solution's conductivity and surface tension, both of which directly affect fiber formation. Higher solution conductivity increases the electric charge carried by the jet, enhancing the electric elongation force. As a result, the fiber diameter decreases due to increased stretching. Equation (2) illustrates this relationship, where the electric current (I) is proportional to charge density.

The applied electric field, determined by the voltage and needle-to-collector distance (Equation 1), must exceed a threshold to initiate jet emission. For larger electric fields, the fiber diameter tends to increase slightly because more fluid is ejected. However, this effect is less pronounced compared to the influence of solution viscosity.

A shorter needle-to-collector distance reduces the jet's elongation time, resulting in thicker fibers. Conversely, increasing the distance allows more time for jet stretching and solvent evaporation, leading to thinner fibers. On the other hand, excessive distances can weaken the electric field, reducing the stability of fiber formation.

Reducing the needle radius or decreasing the flow rate results in thinner fibers. Smaller needle radii create finer initial jets, while lower flow rates reduce the amount of fluid ejected, enhancing the elongation effect.

In addition to these parameters above, the technique is also affected by the environmental conditions, such as the relative humidity and ambient temperature. Higher humidity generally leads to thinner fibers because slower drying allows extended stretching of the jet. Conversely, excessive humidity can prevent proper drying, causing the jet to break into droplets and inhibiting fiber formation. Similarly, temperature affects solvent evaporation rates, with higher temperatures facilitating faster solidification.

Electrospinning is highly adaptable, enabling the creation of nanofibers with intricate structures by varying needle and collector configurations. In coaxial electrospinning, two needles are concentrically aligned, such that one precursor solution can be delivered through an inner capillary while the other can pass through the outer capillary, creating tubular or core-shell fibers. With side-by-side needles bi- or three-phase fibers can be obtained [23,39]. Using rotating drums or parallel threads, aligned fibers can be obtained which is advantageous for applications based on fiber orientation [21,40,41]. Using more complex electrodes such as metallic wires coupled to mobile positioners, liquid collectors and assemblies [23,42,43] three-dimensional structures can be obtained.

3. Composite Ferroelectric and Multiferroic Fibers with Inorganic Inclusions

Recent studies on ferroelectric nanowires have revealed interesting size dependent properties that deviate significantly from their bulk counterparts. These nanostructures not only retain

 doi:10.20944/preprints202501.2184.v1

ferroelectric properties at extremely small diameters, but can also exhibit enhanced axial polarization with decreasing size [44] and significant ferroelectric and piezoelectric responses [45]. This underscores the potential for novel ferroelectric applications of functionalized nanofibers.

X-ray diffraction measurements on $BaTiO_3$, $PbTiO_3$ and PZT ferroelectric nanowires have confirmed the preservation of their polar structure. However, these nanostructures often display reduced spontaneous deformation and tetragonality compared to macroscopic crystals [46]. A key finding is that below the Curie temperature, spontaneous polarization develops parallel to the wire's axis with the [001] direction of the tetragonal structure aligning along this axis [40,47,48]. This alignment has significant implications for the anisotropic properties of these nanowires.

Traditionally, the fabrication of ferroelectric nanowires has relied on complex and costly techniques. In this context, electrospinning emerges as a promising, cost-effective alternative for producing functionalized ferroelectric nanofibers. This technique offers advantages in terms of process control and versatility, enabling the synthesis of a wide range of ferroelectric and multiferroic nanofibers with tailored properties.

This section focuses on the synthesis of composite electrospun nanofibers based on ferroelectric and multiferroic materials. The discussion of ferroelectrics and multiferroics is linked to the deep relationship between them. In particular they share the requirement for good electrical insulation. This characteristic is crucial whether considering intrinsic multiferroics or as composite systems involving multiple materials. By exploring these relationships, we aim to elucidate the potential of electrospinning in creating multifunctional nanofibers with enhanced ferroelectric and multiferroic properties.

3.1. Ferroelectric Polymers

Ferroelectric polymers encompass a wide range of materials, including polylactic acid (PLLA), polylactic glycolic acid (PLGA), and most notably, poly(vinylidene fluoride) (PVDF) and its copolymers [41,49–52]. Among these, PVDF and its derivatives are the best-known and most widely used.

PVDF, particularly in its β phase, exhibits strong ferroelectric properties with a high electromechanical response. The electrospinning technique is especially effective for preparing PVDF nanofibers. Depending on the precursor solution PVDF concentration, nanofibers with diameters in the range 60-400 nm can be prepared [41,49–52]. Notably, electrospinning promotes the formations of the β (polar) phase in PVDF nanofibers, especially in thinner fibers [49,52], due to mechanical elongation and polarization induced by the applied electric field. In PVDF nanofibers the c-axis of crystallites tends to align along the fiber axis enhancing their piezoelectric properties.

Both natural and synthetic polyamides can display ferroelectric properties [53–56], with nylons being the most extensively researched synthetic ferroelectric polyamides [57]. The ferroelectric hysteresis characteristics identified in even-numbered nylons were initially documented in nylon-6 subjected to quenching from the melt, attributed to the autonomous rotation of dipoles within the structurally unstable nematic-type configuration [58]. The molecular mobility of dipolar entities within polyamide 6,9 was systematically investigated using a synergistic approach that combined thermo-stimulated current (TSC) and dynamic dielectric spectroscopy (DDS). Significantly, this study marked a pioneering effort in quantifying polarization and piezo/pyroelectric coefficients, thereby elucidating the distinctive ferroelectric behavior inherent in polyamide-6,9. Ferroelectric activity was detected in nylon-6,9 subsequent to polarization up to 100 MV m^{-1} [59].

Odd-numbered nylons, including nylon-77, nylon-79, nylon-97, and nylon-99, display ferroelectric behavior due to the parallel arrangement of amide dipoles within crystalline regions. This phenomenon mirrors the characteristics observed in nylon comprised of ω-aminocarboxylic acid with an odd number of carbon atoms [60]. Nylon-11, a key odd-numbered nylon, shows promise as a functional material for electronic devices or energy storage [61–63]. It is crucial to control the formation of metastable crystalline phases, such as γ-piezoelectric or δ'-ferroelectric, for these

 doi:10.20944/preprints202501.2184.v1

applications. A recent method was described for manufacturing metastable γ-phase nylon-11 fibers using electrospinning with a customized solvent system [64].

Liquid crystal polymers represent a distinct subclass of ferroelectric polymers. These materials exhibit properties intermediate between conventional liquids and solid crystals. The occurrence of spontaneous polarization is observable in liquid crystals that have a smectic phase, which consists of rod-shaped molecules (mesogens) with a center of chirality [65].

Researchers have developed ferroelectric liquid crystal polymers using bases such as polysiloxanes, polyethers and polyesters, often incorporating side-chains with more than one chiral center or several side-chain structures. These ferroelectric liquid crystal polymers exhibit a wide range of physical properties, making versatile materials with ferroelectric characteristics [66].

Over the past ten years, advanced fiber mats with exceptional functionality and responsiveness have emerged, through electrospinning of polymers incorporating liquid crystals [65,67,68]. The liquid crystal component, responsible for the responsive features, is commonly encapsulated in fibers with a core/sheath structure, manufactured through coaxial electrospinning [69–71]. Alternatively, it can be an integral part of the polymer itself, as seen in liquid crystal elastomers [65,72,73].

3.2. Electrospinning Assisted Ferroelectric Inorganic Nanofibers

Electrospinning has emerged as a versatile technique for producing nanofibers of inorganic ferroelectric materials. The process involves mixing appropriate reagents in precursor solutions along with a transport polymer [25,74]. The morphology and diameter of the nanofibers can be controlled by adjusting the concentrations of the reagents in the precursor solutions [22,25,42,74,75].

To obtain inorganic nanofibers the prepared fiber mats must undergo a heat treatment process. This vaporizes the base polymer, promotes the coalescence and growth of the grains, and stabilizes the ferroelectric phase [42,46,76]. The heating rate must be carefully controlled to allow for slow polymer vaporization and gradual fiber formation. If the vaporization occurs too rapidly, the granular inclusions may not have sufficient time to connect, resulting in powder formation instead of fibers. Table 1 summarizes recent work on the production of inorganic ferroelectric nanofibers using this procedure, along with their respective heat treatment, purpose and potential applications.

Table 1. Ferroelectric nanofibers prepared by electrospinning with ferroelectric granular inclusions. The high temperature procedure that vaporizes the transporting polymer and coalesces the grains to form ferroelectric fibers is indicated, along with the intended purpose and potential applications. PVP - Polyvinylpyrrolidone, PDMS – Polydimethylsiloxane, BNKZ - $Bi_{0.5}(Na_{0.82}K_{0.18})_{0.5}ZrO_3$, KNNS – $(K_{0.48}Na_{0.52})(Nb_{0.95}Sb_{0.05})O_3$, BZT–BCT - $(1-x)Ba(Zr_{0.2}Ti_{0.8})O_3–x(Ba_{0.7}Ca_{0.3})TiO_3$, PAN – polyacrylonitrile.

Polymer	Inclusions	Heat treatment	Purpose	Ref
PVP Mw = 1 300 000	$KNbO_3$	Heated to 550°C, at a 5 °C/min, in air	For humidity sensor	[77]
PVP	$(Na,K)NbO_3$	Dried at 100 °C in nitrogen atmosphere for 12 h. Annealed at 800 °C for 1 h in air	For biocompatible implants and tissue growth	[78]
PVP	$PbZr_{1-x}Ti_xO_3$ (PZT) (52/48)	Annealed at 650°C in air	To measure single-fiber bending piezoelectric voltage	[79]

 doi:10.20944/preprints202501.2184.v1

PVP Mw = 13 000 000	0.96KNNS-0.04BNKZ, BZT-BCT, PZT (52/48)		Energy harvesting	[80]
PVP Mw = 1 300 000	$BaTiO_3$ nanofibers in PDMS	Calcined, 1000 °C, 6h, then inserted in PDMS	Flexible nanogenerator	[81]
PVP Mw = 1 300 000	Aurivillius $Bi_5Ti_3FeO_{15}$	Dried in vacuum overnight at 90 °C. Calcined calcined at 300 °C for 2 h in oxygen burn PVP. Annealed at 600 °C for 2 h in nitrogen. Heating rate of 30 °C/h.	Multiferroic nanofibers	[82]
PVP Mw = 1 300 000	Co doped $Ba_{0.7}Sr_{0.3}Ti_{0.95}Co_{0.05}O_3$	Dried at 130 °C for 4 h, and heated at 400 °C for 2 h Annealed at target temperatures (700 °C and 600 °C) for 2 h under heating rate of 2 °C/min.	Multiferroic nanofibers	[83]
PVP Mw = 1 300 000	$Na_{0.5}Bi_{0.5}TiO_3$ (NBT) nanofibers in PVDF	Dried at 60 °C for 48 h, and then kept at 325 °C and 700 °C for 1 h. Afterwards NBT fibers inserted in PVDF.	NBT-PVDF composites in capacitors, for energy storage applications	[74]
xylene	$Pb(Zr_{0.52}Ti_{0.48})O_3$ (PZT)	The as-spun fibers and mats were isochronally sintered in air for two hours at 400, 500, 600, 700, and 800°C;	To study PZT electrospun nanofiber synthesis.	[84]
PVP	Co-doping of Nb^{5+}-Nd^{3+} into PZT nanoneedles	Calcination at 800 °C for 2 h	For piezoelectric and high dielectric constant applications	[85]
PVP Mw = 1 300 000	vertically aligned ultralong $Pb(Zr_{0.52}Ti_{0.48})O_3$ (PZT) nanowire	Calcination at 650 °C for 3 h	Wearable energy-harvesting and self-powered Devices; Flexible Fiber Nanogenerator;	[86, 87]
PVP	$BaTiO_3$	Pyrolysis in nitrogen at 900 °C	Photocatalysis	[88]

 doi:10.20944/preprints202501.2184.v1

Mw = 1 300 000				
PVP Mw = 1 300 000	$Ba_{0.6}Sr_{0.4}TiO_3$ (BST)	Different heat treatment temperatures: calcined at 600–800 °C for 2 h in air	Study BST synthesis	[89]
PVP Mw = 50 000	$Ba_{0.6}Sr_{0.4}TiO_3$ (BST)	Dried at 60 °C for 10 h. Calcined at 900 °C in air, then included in PVDF to form BST-PVDF composites by drop casting	Nanocomposite capacitors;	[90]
PVP	$LiNbO_3$ (LNO)	Annealing at 700 °C for 6 h;	Study LNO fiber synthesis	[91]
PVP	Mn-doped $LiNbO_3$	Annealing at 700 °C;	Study Mn-LNO fiber synthesis	[92]
PVP	$BaTiO_3$-Multiwalled carbon nanotubes core-shell fibers	Put in vacuum oven at 70 °C for 1 h, and annealed at 800 °C in a nitrogen atmosphere for 2 h	Flexible piezoelectric pressure sensors	[93]
PAN Mw = 150 000	$BiFeO_3$	Calcined at 500 °C for 3 h. Then dispersed in PVDF to form a composite	Flexible piezoelectric nanogenerators	[94]
PVP Mw = 1 300 000	$BiFeO_3$	Thermal annealing at temperatures from 400 to 600 °C for 2 h in ambient conditions	Photovoltaic devices	[95]
PVP Mw = 1 300 000	$BiFeO_3$	Calcined at 520 °C for 2 h in an ambient atmosphere	Photocatalysis	[96]

Among the many ferroelectric materials studied, barium titanate ($BaTiO_3$, BTO) and lead zirconate titanate (PZT) [22,25,42,74–76,84,88,90,93,97,98] have received significant attention.

Barium titanate nanofibers mats have been produced with both aligned and randomly oriented nanofibers morphologies as shown in Figures 2 and 3. The fibers typically have average diameters ranging from 150 to 400 nm and consist of connected BaTiO3 nanoparticles forming long filaments.

 doi:10.20944/preprints202501.2184.v1

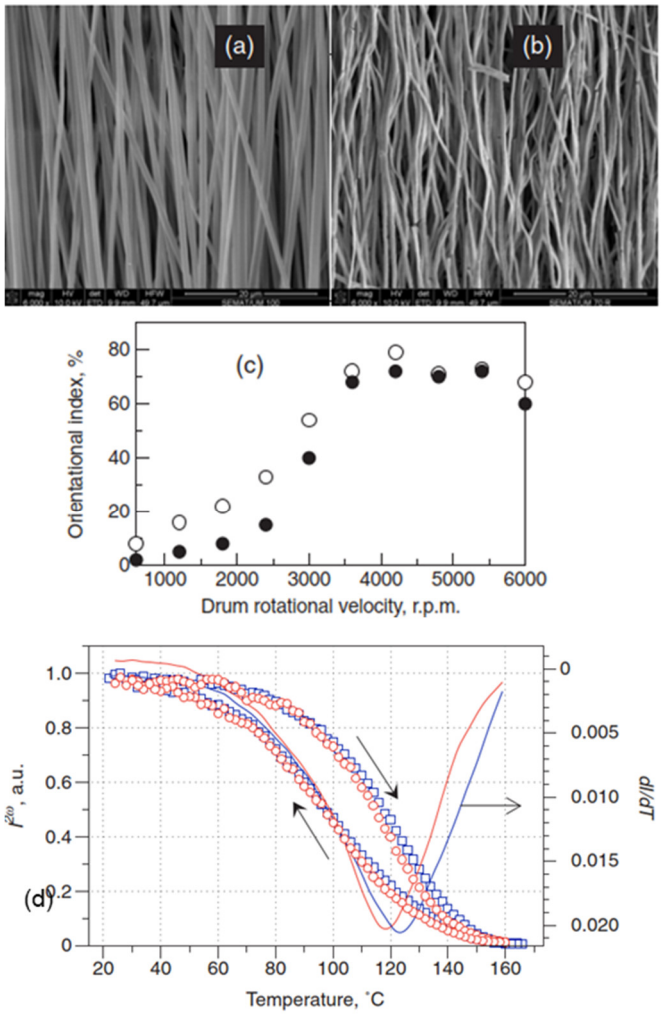

Figure 2. SEM images of the barium titanate fibers (a) As-electrospun and (b) after annealing; (c) evolution of the alignment degree (orientational index) of the nanofibres with the rotation velocity of the collector drum. Open and filled circles correspond to as-electrospun and annealed nanofibres, respectively [42,75,97]. In d) the normalized SHG intensity as a function of temperature observed in nanofibers of $BaTiO_3$ calcined at 900 °C (squares) and 1100 °C (circles). The solid curves are the derivatives of I(T) showing a minimum at the ferroelectric transition temperature of bulk $BaTiO_3$ [76].

 doi:10.20944/preprints202501.2184.v1

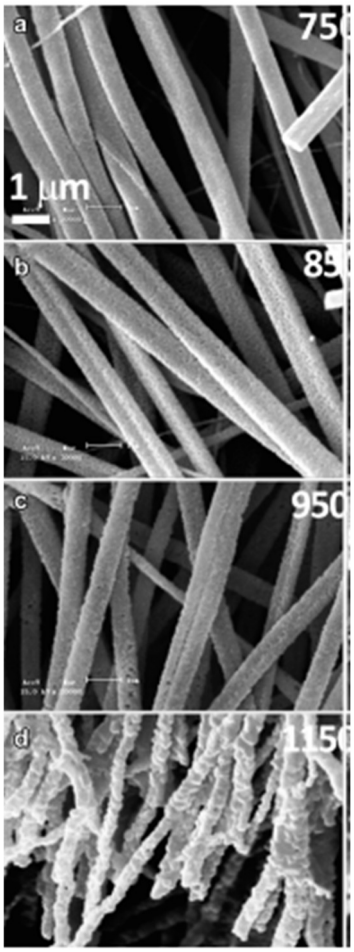

Figure 3. SEM images of the $BaTiO_3$ nanofibers calcined at a) 750 °C, b) 850 °C, c) 950 °C and d) 1050 °C for 6 h [98].

Studies on this type of inorganic ferroelectric fibers have focused mainly on their synthesis and applications. Few studies have demonstrated the existence of ferroelectricity in fibers. Different phases can coexist at room temperature (cubic, tetragonal, orthorhombic) and the reduction to the nanoscale tends to favor the stabilization of the paraelectric, non-ferroelectric cubic phase. From structural measurements and Raman spectroscopy measurements the production of nanofibers with the tetragonal ferroelectric phase was observed for nanofibers annealed in the temperature range 800-1000°C [42,46,75,97,98]. Higher annealing temperatures led to better crystallization of the $BaTiO_3$ nanofibers, but also to rougher nanofiber surfaces with optimized annealing temperatures in the region 900-1000°C.

The temperature dependent second harmonic generation response presented an anomaly in the vicinity of the paraelectric–ferroelectric phase transition (Figure 2d), confirming the change to the ferroelectric phase with decreasing temperature. The existence of domain structure and local switching studied by piezoelectric force microscopy (PFM) present clear evidence of the polar phase at room temperature. Using this feedback, the required conditions were determined to prepare ferroelectric fibers with high alignment and confirm the presence of the ferroelectric phase at room temperature [76].

Taking advantage of the synthesis studies, more recently, barium titanate nanofiber mats have been used as components in the development of piezoelectric nanogenerators [81]. The piezoelectric nanogenerator with $BaTiO_3$ electrospun nanofibers aligned vertically within the polydimethylsiloxane (PDMS) was able to produce an output power of 0.1841 µW with maximum voltage of 2.67 V and current of 261.40 nA under a low mechanical stress of 2 kPa. Additionally, the

 doi:10.20944/preprints202501.2184.v1

system displayed a high dielectric constant of 40.23 at 100 Hz. The harvested energy was sufficient to power a commercial LED directly or alternatively could be stored in capacitors after rectification [81].

Barium titanate electrospun nanofibers have been used as piezoelectric sensors [93,99], as seen in Figure 4. These sensors incorporate barium titanate ceramic nanofiber mats, with a polymer-like softness of 50 mN, a large Young's modulus of 61 MPa, and an elastic strain of 0.9%, resisting fracture after deformation. The nanofiber mats generated a highly sensitive piezoelectric response, producing an output voltage of 1.05 V when subjected to a pressure of 100 kPa with a response time of 80 ms.

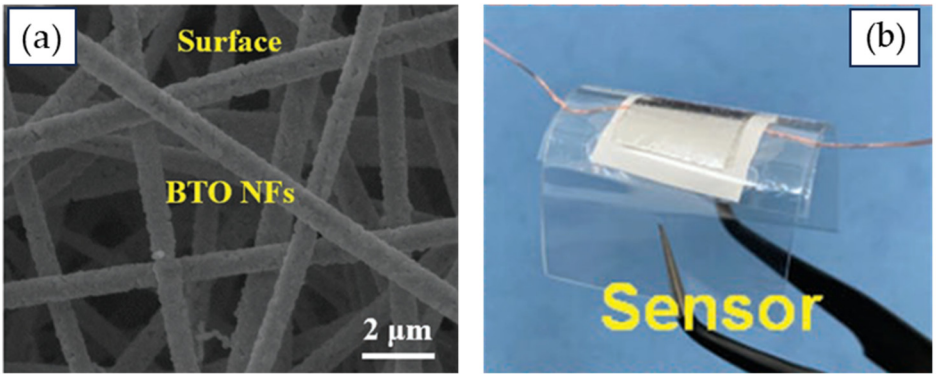

Figure 4. (a,b) Barium titanate flexible nanofiber mat [99].

Beyond pure $BaTiO_3$ fibers, doped barium strontium titanate ($Ba_{0.6}Sr_{0.4}TiO_3$ or BST) [89,90] nanofibers have also been produced with diameters in the range of 100-200 nm. BST is attractive due its large dielectric constant, high tenability, low dc leakage, low loss tangent, and stable operation at high temperature. Higher calcination temperatures promoted improved BST nanofiber crystallinity [89]. The incorporation of BST fibers in a polymeric matrix has been explored for use as nanocapacitors. High energy densities and fast discharge speeds, with improved dielectric permittivity, were obtained making them potentially attractive for energy-storage applications [90].

Bismuth ferrite, $BiFeO_3$, nanofibers have been developed a variety of applications. Their ferroelectric properties were characterized after different annealing temperatures. Their photovoltaic performance displayed enhanced generated voltage generation compared to films [95]. The inclusion of electrospun $BiFeO_3$ fibres inside ferroelectric polymers, such as PVDF has been leveraged to produce flexible piezoelectric energy harvesters [94]. Additionally, the use of $BiFeO_3$ nanofibers in photocatalysis was explored in [96]. They were able to more efficiently degrade pollutants than in the bulk form.

Lanthanum doped bismuth titanate ($Bi_{3.25}La_{0.75}Ti_3O_{12}$, BLT) ferroelectric nanofibers with diameters between 100 nm and 300 nm were fabricated by electrospinning followed by annealing at 700 °C in air for 1 h [100]. Piezoeresponse force microscopy (PFM) measurements of the strain versus voltage hysteresis loops indicated ferroelectricity and an effective piezoelectric coefficient of d_{33} = 61 pm/V was determined, about three times greater than that of a pure BLT film.

Lead zirconate titanate (PZT) ferroelectric nanofibers have been developed for flexible, wearable and self-powered energy harvesters and nanogenerators taking advantage of their significant piezoelectric coefficient [5,86,87,96]. Their synthesis conditions, in particular their annealing treatments, were studied in reference [101]. Typical fiber diameters range from 50-200 nm. Electrospun PZT piezoelectric nanogenerator fiber mats can deliver 1.63 V, with an output power of 0.03 μW [5], while oriented multilayer PZT fibers were stacked together have achieved an ultra-high output voltage of 209 V and current density of 23.5 μA/cm^2 [86,87].

In conclusion, electrospinning-assisted synthesis of ferroelectric inorganic nanofibers offers a promising route for developing advanced materials with tailored properties for various applications in energy harvesting, sensing, and catalysis.

3.3. Electrospinning Assisted Multiferroic Nanofibers

 doi:10.20944/preprints202501.2184.v1

Beyond single-phase ferroelectrics, magnetoelectric (ME) multiferroic materials, which present simultaneous magnetic and electric ordering, have attracted significant scientific and technological interest [102]. These materials hold promise for applications in information storage, sensors, actuators, and low-power energy-efficient electronics [103–107]. However, in single-phase multiferroics, the microscopic mechanisms underlying ME coupling have been challenging to unravel, hindering the development of strong ME responses at useful temperatures [102].

To address these limitations, artificial multiferroic composites combining ferromagnetic (magnetostrictive) and ferroelectric (piezoelectric) materials have emerged as a potential alternative to single-phase multiferroics. These composites present robust magnetoelectric properties [108–110] with ME coupling coefficients up to ~100mVcm^{-1}Oe^{-1} [110]. The strong ME coupling arises from the mechanical interaction between both phases, linking the electric, magnetic, and elastic fields. By carefully selecting the interface geometry and constituent materials, the ME coupling in composites can be engineered and optimized.

Various geometries have been explored for multiferroic magnetoelectric nanostructures, including self-assembled magnetostrictive nanopillars in a piezoelectric matrix, multilayers, and magnetostrictive nanograins in a piezoelectric matrix [102,111]. However, in thin-film structures, substrate clamping can significantly constrain strain-mediated interactions, limiting the achievable ME properties [112]. Interestingly, it has been predicted that substrate free structures, such as nanofibers, can exhibit ME properties several orders of magnitude higher than their thin-film counterparts [112,113].

Composite ferromagnet-ferroelectric nanofibers represent an exciting platform for such applications and can be prepared with various phase morphologies. These include core-shell structures (Table 2), Janus or side by side arrangements (Table 3), and randomly mixed composite configurations (Table 3). In core-shell nanofibers, the ferromagnetic material forms the core, surrounded by a ferroelectric shell. In Janus nanofibers, the ferromagnetic and ferroelectric phases are arranged side-by-side. In composite nanofibers, ferromagnetic and ferroelectric precursors are mixed into a single solution, creating a random distribution of the phases.

All these architectures can be fabricated using electrospinning. Core-shell nanofibers are produced using a dual syringe pump and a coaxial needle. The solution for the magnetic core is pumped through the inner part of the needle while the ferroelectric shell solution is simultaneously pumped through the outer part. Janus fibres can be fabricated with two needles are placed side-by-side and pumping the ferromagnetic and ferroelectric solutions together. For composite fibers, the single mixed solution is pumped through one needle as in conventional electrospinning.

These substrate-free, tunable nanofiber geometries provide a versatile platform to enhance magnetoelectric coupling and broaden the range of functional applications for multiferroic materials.

3.3.1. Core-Shell Multiferroic Fibers

Core-shell composite nanofibers, featuring a magnetic core surrounded by a ferroelectric shell are the most common type of multiferroic nanofibers produced by electrospinning. Various material combinations have been successfully employed to fabricate these nanofibers, including $CoFe_2O_4$-$Pb(Zr_{0.52}Ti_{0.48})O_3$ [114], $NiFe_2O_4$–$Pb(Zr_{0.52}Ti_{0.48})O_3$ [115,116], $NdFeO_3$-$Pb(Zr_{0.52}Ti_{0.48})O_3$ [117], $CoFe_2O_4$-$BiFeO_3$ (see Figure5) [118,119], $NiFe_2O_4$-$BiFeO_3$ [119], $NiFe_2O_4$-$BaTiO_3$ [120], $CoFe_2O_4$-$Ba(Zr_{0.2}Ti_{0.8})O_3$–$0.5(Ba_{0.7}Ca_{0.3})TiO_3$ [121], as summarized in Table 2.

 doi:10.20944/preprints202501.2184.v1

Table 2. Multiferroic core-shell nanofibers prepared by electrospinning. The transporting polymers, high temperature procedure to vaporize the polymer and coalesce the grains to form the fibres is presented, along with the magnetoelectric coefficient, when measured. PVP - Polyvinylpyrrolidone, PMMA – Polymethyl methacrylate, PVA - Polyvinyl alcohol. MD – Magnetodielectric measurements.

Polymer	Core-Shell fibers	Heat treatment	Magnetoelectric Coefficient	Ref
PVP for CFO Mw = 1 300 000 PMMA for PZT Mw = 120 000	$CoFe_2O_4$-$Pb(Zr_{0.52}Ti_{0.48})O_3$ CFO-PZT	Nanofibers were collected on Pt/Ti/SiO2/Si substrates, dried at 120 °C for 4 h, followed by heating at 400 °C and then thermal annealing at 750 °C for 2 h in air	α_{31} = 29.5 V/cmOe	[114]
PVP for NFO and PZT Mw = 1 300 000	$NiFe_2O_4$–$Pb(Zr_{0.52}Ti_{0.48})O_3$ NFO-PZT	Fibers dried at 40 °C for 24 h and annealed in air at 650 °C for 1 h	*Av = δHr /V Av = – 24 Oe/V Converse effect, @ 5.4 GHz [76] MD = Δε′/ε′ MD = 8 % (unassembled), -2 % (assembled in magnetic field) @ 20-22 GHz, H = 0.8 T* [116]	[115,116]
PVP for NDO Mw = 1 300 000 PVA for PZT Mw = 50 000	$NdFeO_3$- $Pb(Zr_{0.52}Ti_{0.48})O_3$ NDO-PZT	Nanofibers were kept on a hot plate to dry at 100 for 10 h, followed by annealing at 850 C for 8 h	-	[117]
PVP for CFO and BFO	$CoFe_2O_4$-$BiFeO_3$ CFO-BFO	Nanofibers were collected to Pt/Ti/SiO2/Si substrates, dried at	*220-250 V/cm Oe* -	[118]

 doi:10.20944/preprints202501.2184.v1

		120 °C for 4 h, followed by thermal annealing at 750 °C for 2 h in air		
PVP Mw = 1 300 000 For NFO and BFO	$NiFe_2O_4$-$BiFeO_3$ NFO-BFO	The samples were dried at 80 °C for 8 h, calcined at 350 °C for 2 h, and then calcined at 700 °C for 4 h, in air.	-	[119]
PVP Mw = 1 300 000 For NFO and BTO	$NiFe_2O_4$-$BaTiO_3$ NFO-BTO	Dried in an oven at 40 °C for 24 h, and then annealed for 1 h at 600–700 °C in air	*0.4 mV/cm Oe @ 30 Hz*	[120]
PVP for CFO and BCZT	$CoFe_2O_4$-$Ba(Zr_{0.2}Ti_{0.8})O_3$–$0.5(Ba_{0.7}Ca_{0.3})TiO_3$ (CFO-BCZT)	Dried at 120 °C for 90 min and calcined at temperatures between 700 °C and 1000 °C, for 1 h.	-	[121]
PVP for BNFO and PZT	$Ba_2Ni_2Fe_{12}O_{22}$-$Pb(Zr_{0.52}Ti_{0.48})O_3$ BNFO-PZT	Dried on a hotplate at 100 °C for 6 h and then annealed at 1100 °C for 6 h	*MD = $\Delta\varepsilon'/\varepsilon'$ MD = –2.4 % @ 100 Hz, H = 0.6 T*	[122]
PVP for CFO and BCTSO	$CoFe_2O_4$–$Ba_{0.95}Ca_{0.05}Ti_{0.89}Sn_{0.11}O_3$ CFO-BCTSO	Fibers dried at 80 °C under vacuum for 12 h and then annealed at 700 °C for 4 h in air	*α = 0.346 V/cm Oe @ H = 1 T*	[123]

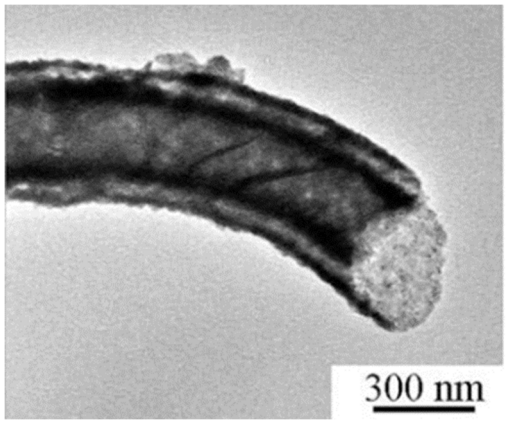

Figure 5. Core-shell nanofibers composed by a CFO core inside a BFO shell [118].

3.3.2. Composite and Janus Multiferroic Fibers

Composite nanofibers with random mixing between both phases and Janus nanofibers have been successfully prepared by electrospinning in the systems such as $Ni_{0.8}Zn_{0.2}Fe_2O_4$-$Ba_{0.7}Sr_{0.3}TiO_3$ [124], $CoFe_2O_4$-$BaTiO_3$ [125], $CoFe_2O_4$-$Pb(Zr_{0.52}Ti_{0.48})O_3$ [126,127], $NiFe_2O_4$–$Pb(Zr_{0.52}Ti_{0.48})O_3$ (see Figure 6) [128], $CoFe_2O_4$–$(Ba_{0.95}Ca_{0.05})(Ti_{0.89}Sn_{0.11})O_3$ [129] and $CoFe_2O_4$- $BiFeO_3$ [130]. A summary of recent work is presented in Table 3.

 doi:10.20944/preprints202501.2184.v1

Table 3. Multiferroic composite and Janus nanofibers prepared by electrospinning. The transporting polymers, high temperature procedure to vaporize the polymer and coalesce the grains to form the fibres is presented, along with the magnetoelectric coefficient, when measured. PVP - Polyvinylpyrrolidone, MOKE – Magneto-optic Kerr effect, SHG – Second harmonic generation.

Polymer	Composite and Janus fibers	Heat treatments	Magnetoelectric Coefficient	Ref
PVP Mw = 1 300 000	$Ni_{0.8}Zn_{0.2}Fe_2O_4$ - $Ba_{0.7}Sr_{0.3}TiO_3$ NZFO-BSTO composite fibers	Composite BSTO/NZFO fibers, with molar ratios of 95/5, 90/10, 80/20 and 70/30, were annealed at 700 °C for 2 h	*MD = Δε'/ε' MD ~18.2% @ 1 kHz, H = 6.3 kOe*	[124]
PVP	$CoFe_2O_4$-$BaTiO_3$ CFO-BTO composite fibers	Composite CFO/BTO fibers with molar ratio 50/50 were dried in an oven at 120 °C for 8 h, followed by annealing at 700 °C for 2 h	α_{31} = 7.8 V/cmOe	[125]
PVP Mw = 1 300 000	$CoFe_2O_4$-$Pb(Zr_{0.52}Ti_{0.48})O_3$ CFO-PZT composite fibers	Composite CFO/PZT fibers with molar ratios 0.75:1, 1:1, and 1.25:1 was dried at 120 °C for 4 h, followed by heating at 400 °C and then annealed at 550 °C for 2 h in air.	-	[126, 127]
PVP Mw = 1 300 000	$NiFe_2O_4$–$Pb(Zr_{0.52}Ti_{0.48})O_3$ NFO-PZT composite fibers	Composite NFO/PZT fibers with molar ratios of 0.75:1, 1:1, and 1.25:1 was dried at 120 °C for 4 h, followed by heating at 400 °C and then annealed at 550 °C for 2 h in air	-	[128]
PVP Mw = 1 300 000	$CoFe_2O_4$–$(Ba_{0.95}Ca_{0.05})(Ti_{0.89}Sn_{0.11})O_3$ CFO–BCTSO composite fibers	Composite BCTSn/CFO fibers with a 1:1 molar ratio was dried at 80 °C under vacuum for 12 h before being annealed at 700 °C for 4 h in an air.	-	[129]
PVP Mw = 1 300 000	$CoFe_2O_4$- $BiFeO_3$ CFO-BFO composite fibers	Molar ratios of 1:0, 1:0.5, 1:1, 1:1.5 and 0:1. The nanofibers were dried at 60 °C for 12 h, followed by heating at 400	-	[130]

 doi:10.20944/preprints202501.2184.v1

		°C for 1.5 h and then annealed at 600 °C for 2 h in air		
PVP Mw = 1 300 000	$CoFe_2O_4$-$BaTiO_3$ CFO-BTO Janus fibers	The fibers were calcined at 750°C for 2 h	*Changes in magnetization at the BTO ferroelectric Curie temperature* [23,131,132] *MOKE [133] Magnetic field-dependent polarization-resolved SHG [134]*	[23,131–135]

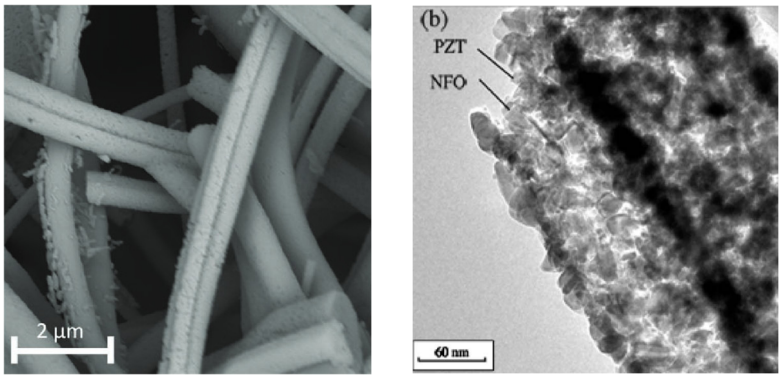

Figure 6. CFO-BTO Janus [134] (left) and NFO-PZT Composite [128] (right) multiferroic nanofibers.

Janus-type biphasic nanowires or nanofibers, characterized by two distinct phases in their hemi-cylindrical sections, have been successfully synthesized [23,131,132]. Unlike core-shell structures where the internal component is inaccessible, Janus-type fibers offer the advantage of exposing both phases while maintaining a substantial interfacial contact area. This unique configuration presents significant potential for enhanced strain coupling in multiferroic nanocomposites. Janus composites of $CoFe_2O_4$-$BaTiO_3$ are particularly interesting and examples are listed in Table 3.

Research on the magnetoelectric (ME) response of electrospun fibers with core-shell, composite, or Janus-type multiferroic structures remains limited. Most studies have primarily focused on processing methods and basic structural characterization, with less emphasis on comprehensive functional property analysis. Despite this, these structures have demonstrated promising multiferroic and magnetoelectric behavior, with ME coefficients ranging from 0.3-29.5 $Vcm^{-1}Oe^{-1}$ (see Tables 2 and 3). This emerging field warrants further investigation.

4. Composite Fibers with Organic Ferroelectric Crystals

Beyond ferroelectric polymers, nanofibers of ferroelectric crystalline materials such as triglycine sulfate (TGS), (1,4-diazabicyclo [2.2.2]-octane) perrhenate (dabcoHReO$_4$) and -glycine have been developed in recent years [24,136,137]. TGS, a well-known ferroelectric material with a Curie

 doi:10.20944/preprints202501.2184.v1

temperature just above room temperature (TC ~ 50°C) is widely used in infrared detectors taking advantage of its high pyroelectricity.

Nanofibers formed from TGS tend to assume a core-shell structure, where the core predominantly consists of the base polymer and the TGS grains form a shell surrounding it. Piezoelectric force microscopy (PFM) and impedance spectroscopy [136,138] established the presence of ferroelectricity in these fibers with a ferroelectric transition temperature close to that of bulk TGS crystals.

Similarly, fibers were synthesized from dabcoHReO$_4$ (1,4-diazabicyclo[2.2.2]-octane perrhenate), a crystalline ferroelectric material known for having the highest spontaneous polarization among water-soluble organic ferroelectrics. Structural, piezoelectric (PFM) and pyroelectric characterization [24] demonstrated their ferroelectric nature and revealed promising pyroelectric and piezoelectric coefficients, making them suitable for nano energy harvesting applications. These fibers achieved a mechanical-to-electrical energy conversion efficiency of approximately 14%, Figure 7, underlining their potential for energy harvesting applications.

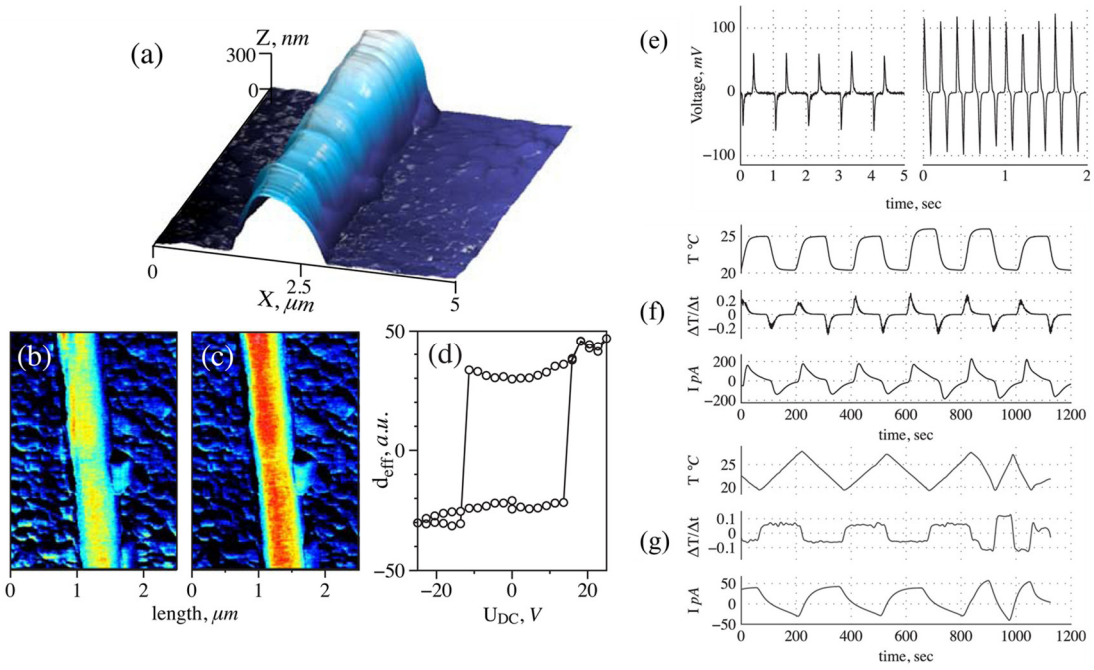

Figure 7. (a) Morphology of the dabcoHReO$_4$ individual fiber obtained by AFM; (b) vertical and (c) lateral PFM-images of dabcoHReO$_4$ nanofibers; (d) piezoelectric response hysteresis loop; (e) Voltage output of the fabricated nanofiber mat under 1 Hz (left) and 5 Hz (right) repeated compressive impacts. Nanofiber mat thickness of 100 μm, working area of 1 cm^2. The temperature cyclic change, derivative and output pyroelectric current obtained in dabcoHReO4 nanofiber mat at pulsed (f) and ramp (g) temperature changes [24].

Electrospun composite nanofibers functionalized with a benzothiazole derivative (BZT 1), incorporating an arylthiophene π-conjugated bridge, dispersed in a poly L-lactic) acid (PLLA) matrix, were successfully synthesized [139]. These fibers were characterized for their linear and nonlinear optical properties as well as their piezoelectric and ferroelectric behavior.

Evaluation of the first molecular hyperpolarizabity β, revealed that BZT 1 is an efficient second-harmonic generator. Local piezoelectric measurements confirmed that the heterocyclic system crystallizes in a nanocrystalline acentric structure when embedded in electrospun nanofibers. Measurements of piezoelectric hysteresis loops via PFM enabled the study of local domain switching under an applied external electric field. The observed out-of-plane hysteresis loop provided direct evidence for the switching of polarization in BZT 1 nanofibers and its ferroelectric properties.

The BZT 1 compound displays a high fluorescence quantum yield of 0.58, Figure 8b). Figures 8d) and 8e) present the PFM images obtained from a single BZT nanofiber deposited on a conductive

 doi:10.20944/preprints202501.2184.v1

substrate. The first image shows the as-electrospun nanofiber before any external polarization field was applied. In the next two images (Figure 8d–e), the out-of-plane PFM contrast is observed after applying +100 V (image d) and then -100 V DC voltage (image e) to the conductive cantilever tip for 10 s. The pronounced contrast in the PFM images arises from an induced deformation in response to the applied ''read'' ac electric field and represents the components of fiber's polarization vector P . This contrast is roughly proportional to the longitudinal piezoelectric coefficient and is determined by the projection of the polarization vector normal to the substrate. The phase, φ, of the signal depends on the orientation of the polarization. ''Bright'' contrasts in the measured A.cos(φ) signal indicate that the polarization lies in the substrate plane, while the dark contrasts correspond to the polarization pointing downward to the surface.

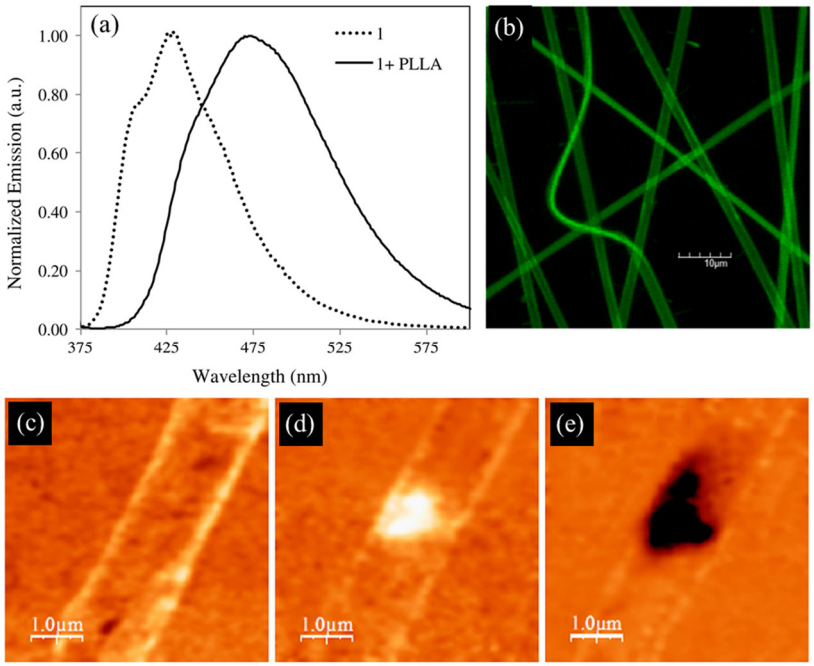

Figure 8. (a) Normalized emission spectra of BZT nanofibers and the pure compound in absolute ethanol; (b) single-photon fluorescence image (50 × 50 μm) of BZT 1 nanofibers. The fluorescence was observed in the wavelength range of 430 – 470 nm following excitation at a wavelength of 405 nm. Vertical PFM images observed in an individual BZT nanofiber: (c) as-electrospun nanofibers (before poling), (d) PFM image after applying a voltage of +100 V at the fixed tip during 10 s, (e) image after applying a voltage of −100 V [139].

The corresponding effective piezoelectric coefficient was estimated to be d_{33} = 20 pm/V, comparable to the piezoelectric coefficient of a poled poly(vinydelenefluoride) film and dabcoHReO$_4$ nanofibers [24]. The switching of polarization confirms the ferroelectric nature of BZT 1, consistent with an acentric crystalline structure. Ferroelectricity is only possible in polar crystallographic point groups lacking a center of inversion [140].

Lead-free organic ferroelectric perovskite nanocrystals (MDABCO-NH_4I_3) were integrated into polymer fibers via electrospinning for mechanical energy harvesting [141], as illustrated in Figure 9. These molecular ferroelectrics, offering structural diversity and easy fabrication, exhibit piezoelectric and ferroelectric properties within the organic-inorganic hybrid materials category. The resulting flexible nanofibers act as effective piezoelectric energy harvesters, achieving an effective piezoelectric voltage coefficient, $g_{eff,}$ of 3.6 VmN^{-1} and emitting blue luminescence at 325 nm. During the ferroelectric–paraelectric phase transition, embedded MDABCO-NH_4I_3 perovskite nanocrystals display a pyroelectric coefficient comparable to state-of-the-art bulk ferroelectric materials. Moreover, these polymer embedded nanocrystals maintain stable piezoelectric output, resisting

 doi:10.20944/preprints202501.2184.v1

oxidation-induced degradation. This durability, combined with their flexible nature, positions these nanocrystal systems as promising candidates for energy harvesting applications.

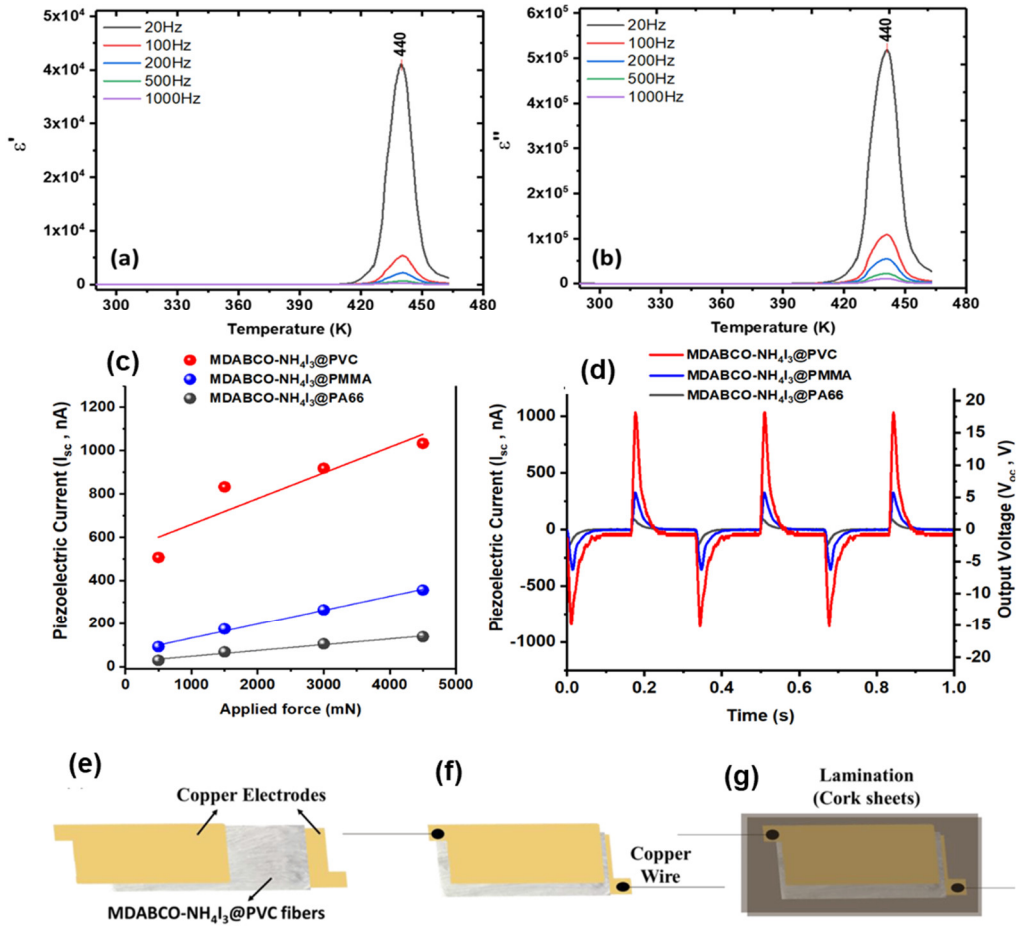

Figure 9. (a) Dielectric permittivity of an MDABCO-NH_4I_3 polycrystalline sample showing its (a) real and (b) imaginary parts as functions of temperature and frequency. The ferroelectric–paraelectric phase transition occurs at 440 K; (c) Piezoelectric current as a function of the applied forces and (d) Output voltage and current as a function of time from MDABCO-NH_4I_3 incorporated into different electrospun polymer nanofibers; (e,f,g) Schematic of MDABCO-NH4I3@PVC piezoelectric nanogenerator [141].

5. Nonlinear Optical Nanofibers

Polymer-based nonlinear optical (NLO) and electro-optical (EO) materials offer an innovative alternative to conventional inorganic crystalline materials, such as lithium niobate ($LiNbO_3$, LBO) and potassium dihydrogen phosphate (KH_2PO_4, KDP), for device applications. Polymeric materials possess several unique features that have driven research in the field. One notable advantage is their low spectral dispersion in the refractive index over a broad range of the electromagnetic spectrum. This characteristic enables the development of traveling-wave infrared modulators operating at exceptionally high modulation frequencies, exceeding 100 GHz, while maintaining relatively long interaction lengths (up to 1 cm). Another advantage of polymeric materials is that they facilitate the fabrication of robust, low-cost optoelectronic devices through monolithic integration with semiconductor electronics.

The electrical and optical properties of organic materials can be tailored through organic synthesis, allowing for the incorporation of chromophores with significant NLO properties. This results in materials with large EO coefficients and low drive voltages. Controlling molecular morphology and dipole orientation is critical for optimizing the performance of NLO organic devices.

 doi:10.20944/preprints202501.2184.v1

In polycrystalline materials with randomly oriented molecules, the net effective dipole moment is negligible, limiting their utility [142].

Electrospinning provides a technique to achieve strong molecular orientation within polymeric fibers, which significantly enhances their anisotropic properties. Organic molecules embedded in electrospun fibers can exhibit high degrees of molecular order, enabling their application in nonlinear optics. [143].

An alternative method to force a macroscopic molecular orientation in polycrystalline NLO materials is the polling of polymers doped with NLO molecules by application of an strong external DC electric field. Here, the guest-host polymer is heated above its glass transition temperature and subsequently placed in a strong electric field before cooling. The molecular orientation of the NLO chromophores is then frozen during the subsequent cooling process. While effective, this method often results in significant chromophore relaxation after electric field removal, leading to decreased anisotropic properties.

In contrast, the electrospinning technique is a powerful tool for controlling the morphology and orientation of polymer chains and the embedded crystalline NLO molecules mitigating relaxation issues. It can be employed with a variety of different polymers and molecular complexes [144].

In one of the earliest examples, Isakov et al. [21] obtained strongly anisotropic optical second harmonic generation based on highly aligned nanofibers of 2-methyl-4-nitroaniline $C_7H_8N_2O_2$, MNA) embedded in poly(L-latic acid) (PLLA) nanofibers, fabricated by the electrospinning technique, Figure 10 a). MNA, a derivative of 4-nitroaniline or para-nitroaniline ($C_7H_8N_2O_2$, pNA), achieves noncentrosymmetric crystallization by substituting a hydrogen atom with a methyl group at the 2-position of the benzene ring. Crystals of MNA exhibit a very large phase matched second harmonic generation (SHG) with a figure of merit over 2 orders of magnitude greater than that of lithium niobate [142].

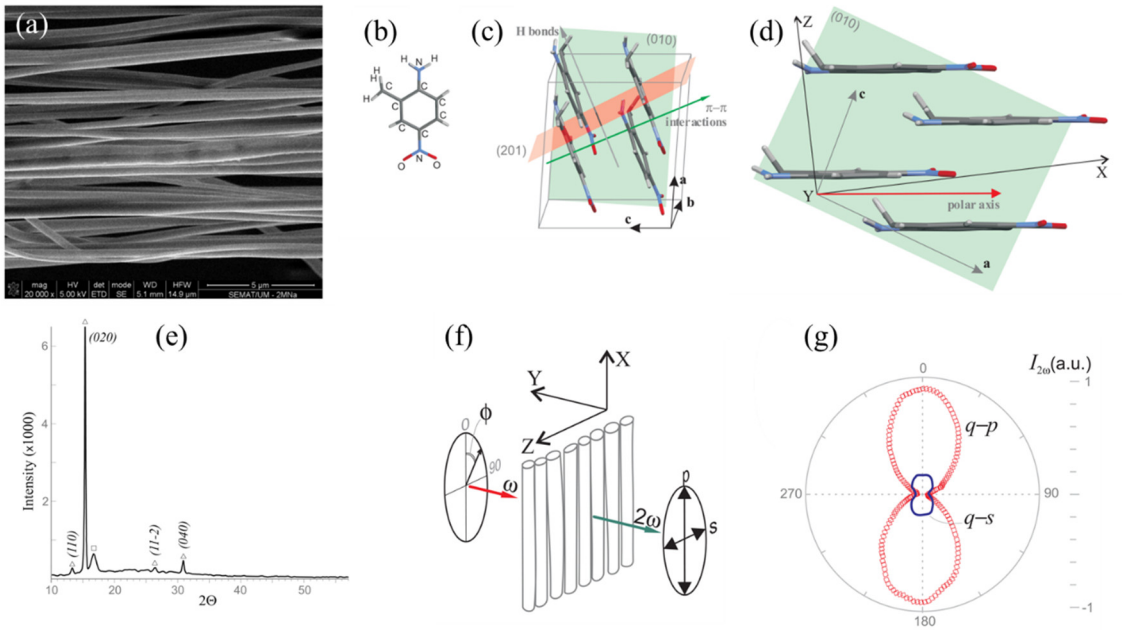

Figure 10. (a) SEM image of MNA@PLLA nanofiber arrays; (b) the MNA molecule ; (c) MNA molecular packing and (d) its projection on the (010) plane (d); (e) XRD pattern of MNA_PLLA fiber arrays; (f), (g) Sketch of the SGH ellipsometry experiment and SHG polarization patterns in the in-plane aligned array of the MNA@PLLA fibers [21]. Here the generated second harmonic light, which passed through an analyzer was oriented either parallel (q-p configuration, q indicates an incident polarization angle) or perpendicular (q-s configuration) to the longitudinal axis of the aligned fibers.

X-ray diffraction analyses revealed that MNA molecules within the electrospun fibers predominantly crystallized with their (010) crystallographic planes parallel to the fiber plane, Figure

 doi:10.20944/preprints202501.2184.v1

10 e). Second harmonic generation polarimetry, shown in Figures 10 f) and 10 g), confirmed a high degree of anisotropy in an array of MNA_PLLA electrospun nanofibers with an effective nonlinear susceptibility coefficient estimated to be 148 pm/V. The signal generated by a mat of MNA_PLLA fibers is as strong as in bulk MNA, highlighting the potential of these nanofibers for a variety of NLO applications. Furthermore, the NLO response was strongly correlated with the size of the MNA nanocrystals within the polymeric fiber host, which could be tuned by adjusting the electrospinning processing parameters. Over the range explored the nonlinear optical response of the electrospun nanofibers of MNA varied by an order of magnitude [145].

High resolution confocal laser scanning microscopy, Figures 11a) and 11b), demonstrated that MNA nanocrystals are homogeneously distributed within the PLLA polymer fiber with particle sizes below 100 nm [145]. The mean MNA crystallite size varies with the fiber diameter: thinner fibers contain smaller crystallites. The SHG efficiency of the nanofibers varied with fiber diameter, showing reduced efficiency when the diameter approached the optical coherence length, due to phase mismatch effects, Figure 11c).

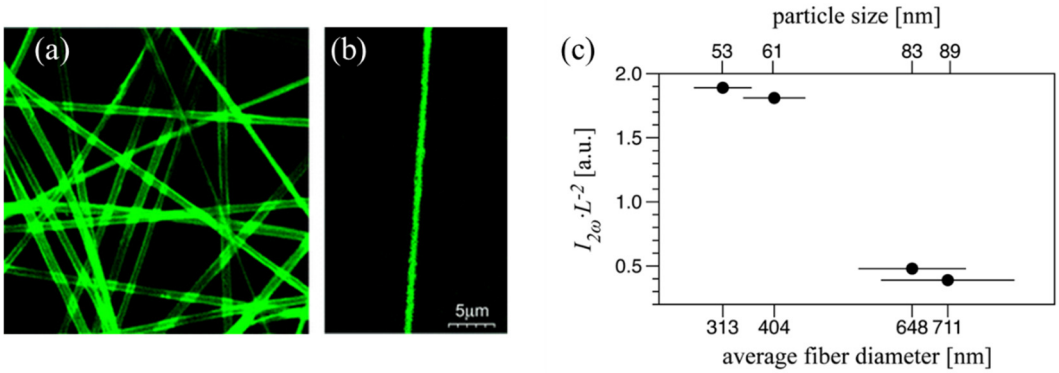

Figure 11. (a), (b) Single-photon fluorescence image of MNA-PLLA nanofibers showing a uniform distribution of MNA nanocrystals embedded within the PLA nanofiber. The excitation wavelength was 405nm and fluorescence was observed in the range of 430-470nm; (c) SHG efficiency of MNA-PLLA nanofibers as a function of the average fiber diameter and MNA particle size [145].

Similar advances have been made using para-nitroaniline (pNA), a prototype molecule for organic NLO materials. It has a delocalized π-π* electron system and unsaturated bridge linking a donor amino group (NH_2) and an acceptor nitro group (NO_2). Despite its large molecular hyperpolarizability [146–148], bulk pNA crystals belong to the centrosymmetric space group $P2_1/n$, preventing macroscopic second harmonic generation [149]. Embedding pNA into electrospun fibers overcame this limitation, as the process induced highly oriented mesocrystalline structures with a dominant acentric surface as shown in Figure 12 [150,151].

Preprints.org (www.preprints.org) | NOT PEER-REVIEWED | Posted: 29 January 2025 doi:10.20944/preprints202501.2184.v1

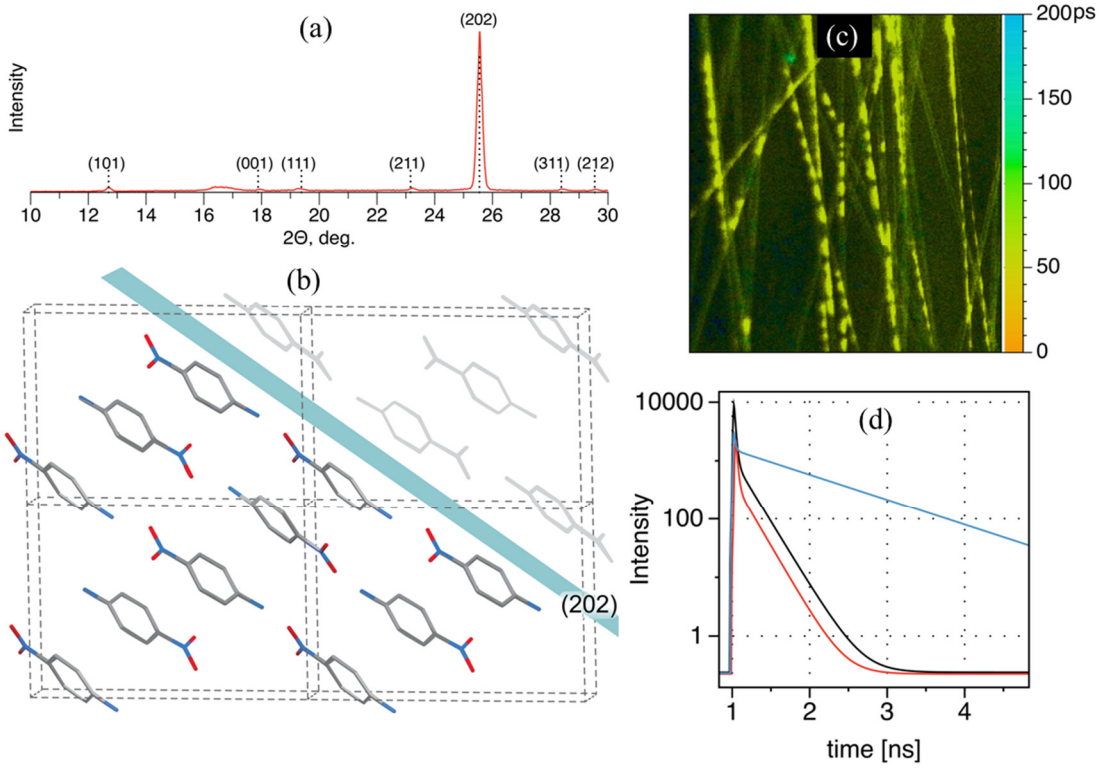

Figure 12. (a) X-ray diffraction pattern revealing strong orientation observed in *p*NA mesocrystalline structure produced by electrospinning; (b) Four unit cells of *p*NA with shown (202) plane terminated the periodic crystal lattice by the surface; (c) 50 × 50 μm micrograph of *p*NA nanofibers obtained by Fluorescence lifetime Imaging Microscope and; (d) double exponential fluorescence decay obtained from *p*NA single crystal (black curve), nanofibers (red curve) and solution (blue curve) [150].

During the electrospinning process, *p*NA was incorporated into PLLA polymer fibers with a strong preferred crystallographic orientation. The X-ray diffraction pattern was dominated by the (202) Bragg reflection which was two orders of magnitude more intense than all the other observed reflections. However, all Bragg reflections could be assigned to the known centrosymmetric crystalline structure indicating that it was not a polymorph.

NLO measurements performed on a single fiber concluded that the effective mean nonlinear optical coefficient d_{eff} was around 42 pm/V, twice that of the highest coefficient measured on meta-nitroaniline or 3-nitroaniline (*m*NA or 3NA) crystal, $d_{33} = 21$ pmV^{-1}, an established SHG crystalline compound. The results demonstrate the possibility of engineering a nanofiber array of centrosymmetric nanocrystals with a strong SHG response comparable to that of single non-centrosymmetric organic crystals. The observed effect resulted from the multiple crystal surfaces having a common orientation with highly aligned molecules forming a head-to-tail dipolar arrangement. Fluorescence lifetime microscopy, Figure 12c) indicate the presence of strong excitonic coupling between molecular units within the fibers and also in bulk *p*NA crystals.

Another example involves 3-nitroaniline (3NA) nanocrystals embedded in poly-ε-caprolactone (PCL), 3NA@PCL, fibers, displayed in Figure 13. The X-ray diffractogram of a 3NA@PCL nanofiber mat revealed that the (400) Bragg peak was the most intense, a notable contrast to the corresponding diffraction pattern from a bulk polycrystalline sample (Figure 13a). This indicates a strong preferential orientation within the fiber mat (Figure 13b). In the crystal unit cell, 3NA molecules are organized such that their molecular dipole moments (represented by arrows) collectively align to produce a net dipole moment parallel to (400) plane, orientated along the polar axis. In the fibers, the (400) plane aligns parallel to the surface of the fiber mat surface, so that the polar axis is directed

 doi:10.20944/preprints202501.2184.v1

along the longitudinal fiber axis. This preferential orientation arises due to the strong electric field applied during the electrospinning process, which aligns the high molecular dipole moments within the fibers.

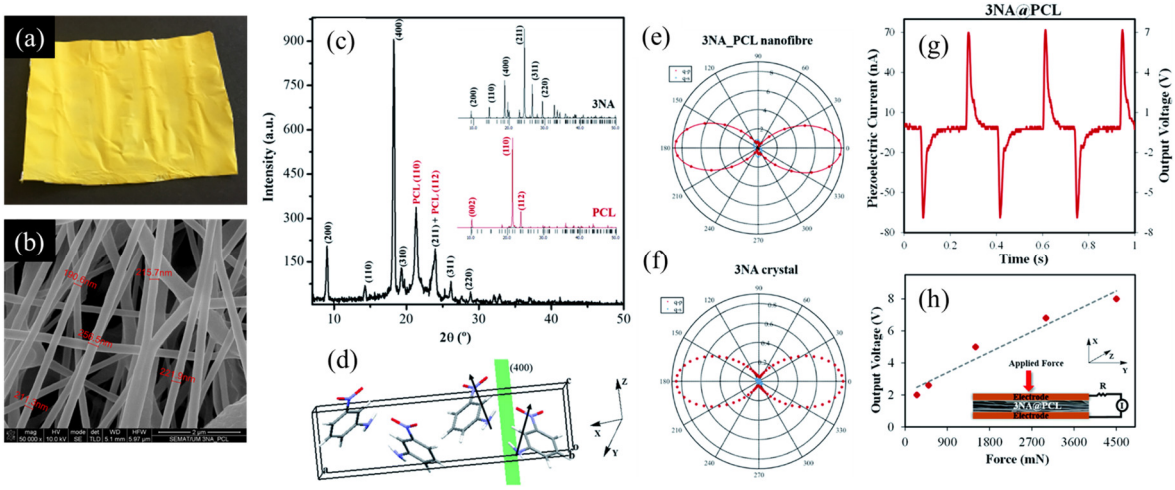

Figure 13. (a) 3NA@PCL electrospun fiber mat deposited on a substrate; (b) Corresponding SEM image; (c) Measured X-ray diffraction pattern of a 3NA@PCL nanofiber mat (the insets show the calculated powder patterns for crystalline 3NA and PCL polymer); (d) Unit cell of 3NA showing the molecular dipoles (represented by arrows) adding to a net dipole parallel to (400); (e) Polar plot of SHG polarimetry data collected on a single 3NA@PCL electrospun nanofiber for *q–p* and *q–s* configurations. (f) Polar plot of SHG polarimetry data collected on a (100) 3NA crystal platelet for *q–p* and *q–s* configurations. The radial axis values are expressed in unit of Counts. The maximum of intensity corresponds to the case where the polarization of incident and emitted light is parallel to each other and aligned with the fiber longitudinal axis; (g) Output voltage and current measured on a 3NA@PCL electrospun fiber mat (h) Plot of ouput voltage versus applied force with a schematic piezoelectric setup of a 3NA@PCL fiber mat. There is a linear relationship between the measured output voltage and the applied force [26].

The anisotropy of polarity curves measured on a nanofiber array and on a (100) oriented 3NA single crystal platelet, under identical excitation conditions, confirm the preferred orientation of the nanocrystals embedded into the fibers (Figure 13c). Notably the effective second order susceptibility measured on a single nanofiber was $d_{eff}^{3NA@PCI} = 80\ pm/V$, four times greater than $d_{eff}^{3NA} = 21\ pm/V$, the corresponding value for macroscopic 3NA crystals [26]. Consequently, the push-pull nitroaniline derivatives embedded within each fiber act as enhanced, polarized nanoemitters of second harmonic generation (SHG) light. Furthermore, the nanocrystals within the fibers are significantly smaller than the optical coherence length of a 3NA platelet crystal (approximately 10 μm), enhancing the SHG output intensity compared to bulk 3NA since phase mismatch is insignificant in the fibers.

Beyond their nonlinear optical (NLO) properties, 3NA@PCL nanofiber mats also function as electric power sources via the piezoelectric effect. Applying a periodic force induces polarization within the acentric crystalline material, enabling an external electric current to flow between the opposite faces of the mat through a load resistance (Figures 13g and 13h). As illustrated in Figure 13g), a periodic force of 3 N generated a voltage and current of up to 7 V and 70 nA, respectively, yielding an instantaneous power density of 122 nW/cm² [26].

Another push-pull molecule closely related to *p*NA is 2-amino-4-nitroaniline, (2A4NA, $C_6H_7N_3O_2$), which, like MNA, is an engineered molecule obtained by replacing a meta-hydrogen on the benzene ring by an amino group [152]. The NLO response of electrospun fibers mats composed by 2A4NA grains inside PLLA polymeric fibers (see Figure 14) were investigated and compared with 3NA crystals under identical conditions [153].

 doi:10.20944/preprints202501.2184.v1

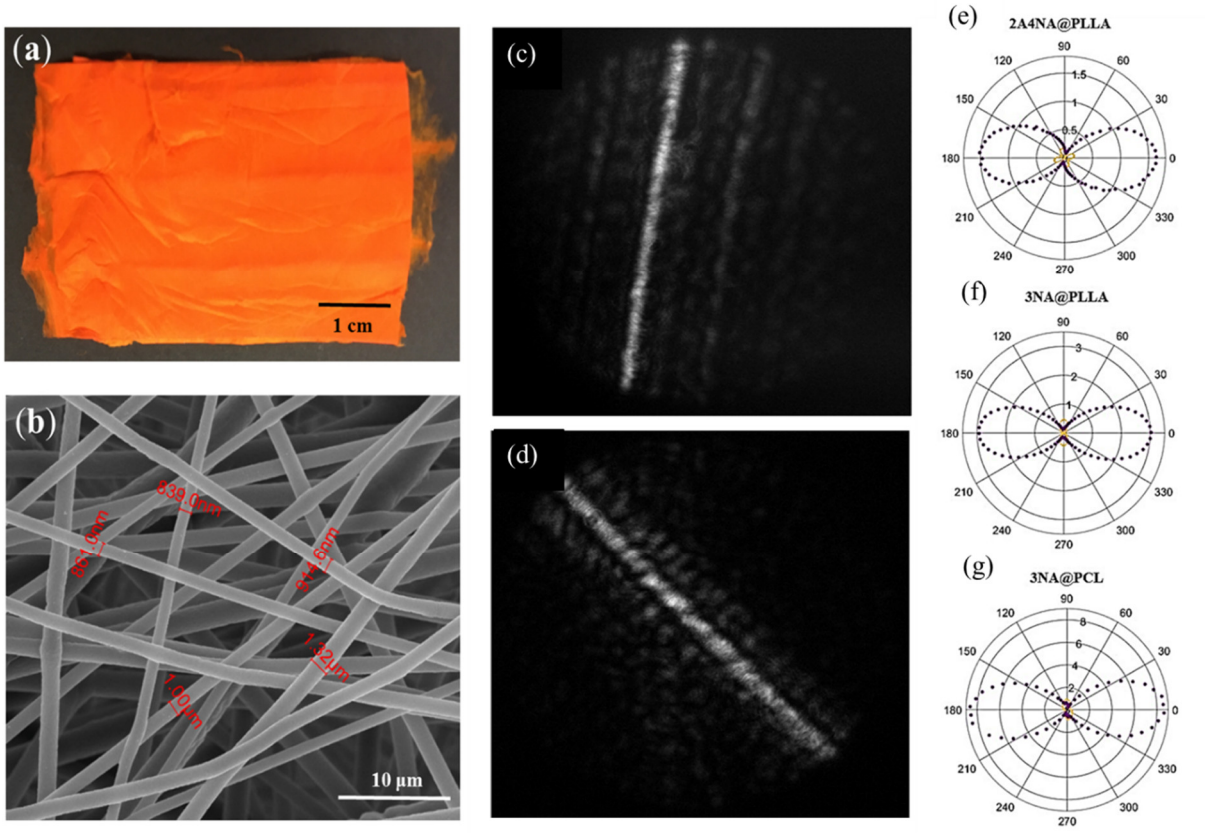

Figure 14. (a) Electrospun 2A4NA@PLLA fiber array deposited on a substrate, (b) corresponding scanning electron microscope image. Monochromatic images of the second harmonic light emitted by single fibers of (c) 3NA@PLLA and (d) 2A4NA@PLLA. Polar plots of SHG polarimetry data collected on a single nanofiber of (e) 2A4NA@PLLA, (f) 3NA@PLLA and (g) 3NA@PCL [26], for q – p and q – s configurations. The radial axis values are expressed in units of 106 Counts [153].

The average diameter of the electrospun 2A4NA@PLLA fibers was 770 nm. X-ray diffraction (XRD) patterns revealed a preferred orientation of 2A4NA and MNA nanocrystals within the polymer fibers. This orientational order was further confirmed by the anisotropy observed in SHG polarimetry curves. For both 2A4NA@PLLA and 3NA@PLLA, the q-p configuration yielded a maximum intensity nearly an order of magnitude higher than the q-s configuration. For comparison, Figure 13e) shows the polarimetry curves measured on an individual 3NA@PCL fiber under the same excitation conditions [26]. Both the 3NA@PLLA and 3NA@PCL fibers exhibited nearly identical anisotropic SHG responses, suggesting that the polymer matrix does not significantly alter the orientational distribution of the nanocrystals. There is negligible optical damage of the nanofibers during the acquisition as the curves possess symmetric maxima, and close on themselves. The nanofibers are optically robust to laser damage.

The estimated effective second-order susceptibility coefficient for 3NA@PLLA was $d_{eff}^{3NA@PLLA} = 56\ pm/V$, which is 1.5 times smaller than that measured for a 3NA@PCL nanofibers, $d_{eff}^{3NA@PCL} = 80\ pm/V$ [26]. For 2A4NA@PLLA the estimated effective second-order susceptibility coefficient was $d_{eff}^{2A4NA@PLLA} = 42\ pm/V$, which is among the highest values reported for organic crystals formed by simple pNA derivative push-pull molecules. The spatial distribution of second harmonic emitters within single 3NA@PLLA and 2A4NA@PLLA fibers is displayed in Figures 14c) and 14d). The 3NA@PLLA fibers showed a relatively uniform distribution of SHG emission along the excited fiber, whereas the SHG emission from a 2A4NA@PLLA fiber is punctuated by intense spots.

Finally, in addition to charge transfer push-pull molecules, electrospun nanofibers embedded with urea, a well-known organic crystalline material, have been produced from precursor solutions

 doi:10.20944/preprints202501.2184.v1

with two different polymers: poly(ethylene oxide) (PEO) and poly(vinyl alcohol) (PVA). Both polymers are very soluble in water, as is urea.

Urea was one of the first organic NLO crystals available commercially. Its nonlinear optical properties been extensively studied due to its simple structure and strong second-harmonic generation (SHG) response. n its bulk crystalline form, urea exhibits an effective second-order nonlinear coefficient approximately 2.5 times greater than that of potassium dihydrogen phosphate (KDP), a widely used inorganic crystal.

With PEO, highly crystalline and orientated nanofibers containing two different polymeric host–guest inclusions were formed, Figure 15. They are the stable α complex and the metastable β complex [154,155].

The α complex has a (PEO)4–(urea)9 stoichiometry [156], and fibers were successfully prepared from a gel-like suspension of a previous inclusion compound (IC) co-crystallized complex. These highly oriented and well-aligned fibers displayed a strong molecular orientation with PEO chains confined inside urea channels. This strong molecular orientation inside the fibers was attributed to a reorientation of rigid crystalline units during the electrospinning process [157]. Remarkably, the electrospinning process stabilized the metastable β phase with a (PEO)3–(urea)2 stoichiometry resulting in an orthorhombic crystal structure as determined from the X-ray diffraction data [155].

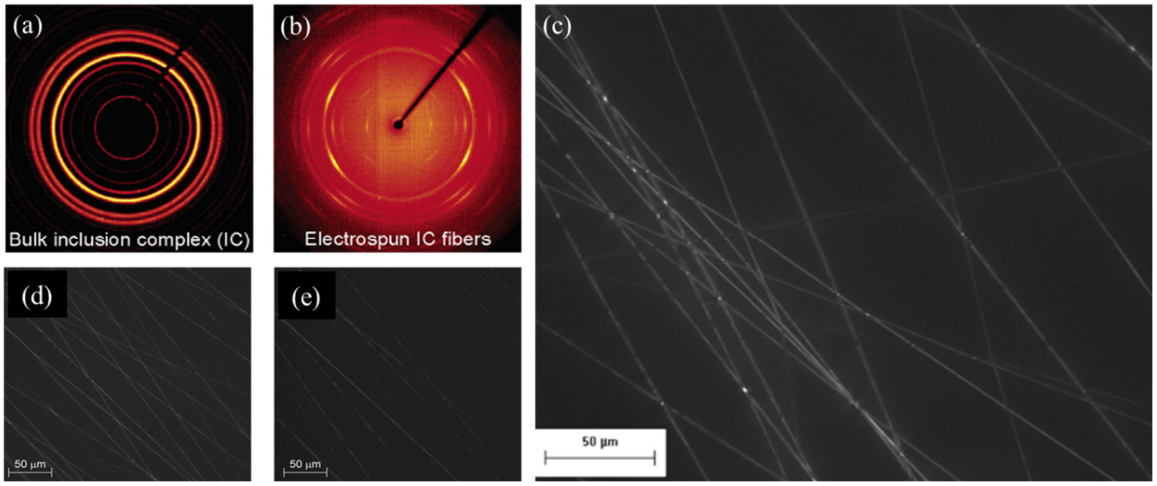

Figure 15. (a) Wide-angle X-ray diffraction 2θ diagrams for (a) the bulk PEO–urea inclusion complex (IC) and (b) electrospun fibers. (c) Crossed-polarized optical micrograph of electrospun fibers of the PEO–urea inclusion complex [157]. Representative crossed-polarized optical micrographs of fibers prepared by electrospinning solutions with (d) 4:9 and (e) 3:2 PEO:urea molar ratios [155].

Unlike the PEO-urea fibers, the PVA-urea nanofibers (1:1 polymer-to-urea mass ratio) show no evidence of inclusion complexes in their X-ray diffraction patterns. Instead, urea nanocrystals inside the PVA matrix retained the tetragonal structure of bulk urea crystals (Figure 16). However, the nanocrystalline urea within the fibers displays a strong preferential orientation with their (110) plane parallel to the fiber mat plane, Figure 16c).

 doi:10.20944/preprints202501.2184.v1

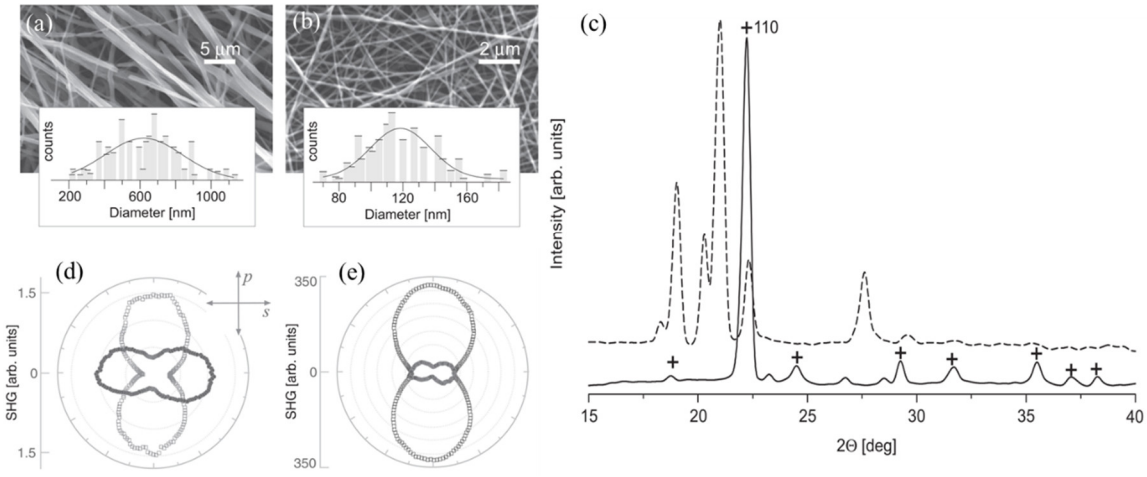

Figure 16. (a) SEM micrographs and thickness distribution of electrospun PEO-urea and (b) PVA-urea nanofibers. (c) X-ray diffraction patterns of electrospun fibers of PEO-urea (dashed line) and PVA-urea (solid line). Crosses indicate diffraction peaks of pure crystalline urea. (d), (e) SHG polarimetry curves of PEO-urea and PVA-urea nanofibers, respectively [143].

The SHG response of urea was quite different in these two polymer fibers. In urea-PVA nanofibers, the urea nanocrystals generated a SHG response as intense as a pure urea powder with an average grain size of 110 μm. The SHG response of isotropic PEO-urea fibers was about two orders of magnitude less than the urea-PVA fibers, Figures 16d) and 16e). However, no SHG signal was observed from urea-Peo fibers. These findings highlight the importance of the host polymer and the resulting crystal structure in determining the nonlinear optical properties of urea-embedded nanofibers.

Although the above results are encouraging, further research is needed to elucidate the mechanisms behind the differing SHG responses and to optimize the fabrication processes for enhanced nonlinear optical properties of organic nanocrystals embedded in polymeric electrospun fibers. Deeper insights into the process will facilitate the development of novel materials with tailored nonlinear optical characteristics

6. Conclusions

In conclusion, this review highlights the promising potential of the electrospinning technique in fabricating multifunctional ferroelectric based nanofibers from a diverse array of materials, including inorganic, semi-organic and all organic compounds. By carefully selecting an appropriate polymer matrix, these materials can be transformed into nano and micro structured hybrid functional systems. These hybrid systems encompass a range of functional materials including piezoelectric ceramics, inorganic ferroelectrics, single-phase ferroelectrics and magnetoelectric multiferroic materials, which exhibit simultaneous magnetic and electric ordering. Among the semi organic crystals, particular emphasis was placed on triglycine sulfate (TGS) due to its technological significance.

In the realm of nonlinear optics, fabrication of nanomaterials in the form of nanofibers using chromophores with high molecular hyperpolarizabilities offers an innovative alternative to conventional inorganic crystalline materials for device applications. In particular, nanofibers incorporating push-pull nitroaniline derivatives have demonstrated enhanced optical second harmonic generation, and have strong potential as nanoscale emitters of polarized light.

Additionally, crystalline hybrid nanofiber mats with pronounced piezoelectric properties have been developed, capable of efficiently converting modest applied forces into significant electrical outputs, generating appreciable piezoelectric voltages.

 doi:10.20944/preprints202501.2184.v1

Looking forward, the quest for cost-effective sensors, actuators, and electronic and photonic components, alongside the increasing demand for device miniaturization and integration, positions electrospun nanofibers as a promising solution. The integration of multiple functionalities into a single nanostructure using the electrospinning technique allows researchers to addresses the key requirements of affordability, flexibility, and versatility when seeking to develop novel multifunctional device technologies.

Author Contributions: writing-original draft preparation, R.M.F.B., E.d.M.G., B.A.; writing-review and editing, R.M.F.B., E.d.M.G., B.A. and M.B.

Funding: This research was funded by Fundação para a Ciência e Tecnologia through FEDER (European Fund for Regional Development)-COMPETE-QREN-EU (ref. UID/FIS/04650 Centro de Física das Universidades do Minho e Porto), PTDC/NAN-MAT/0098/2020, and 2022.03564.PTDC.

Acknowledgments: R.M.F.B. acknowledge financial assistance by national funds (OE), through FCT − Fundação para a Ciência e a Tecnologia, I.P., through DL 57/2016/CP1377/CT0064 (DOI: 10.54499/DL57/2016/CP1377/CT0064).

Conflicts of Interest: The authors declare no conflict of interest.

References

1. Sekhar, M.C.; Veena, E.; Kumar, N.S.; Naidu, K.C.B.; Mallikarjuna, A.; Basha, D.B. A review on piezoelectric materials and their applications. *Cryst Res Technol* **2023**, *58*, 2200130.
2. Lines, M.E.; Glass, A.M. *Principles and applications of ferroelectrics and related materials*; Oxford university press: 2001.
3. Setter, N.; Damjanovic, D.; Eng, L.; Fox, G.; Gevorgian, S.; Hong, S.; Kingon, A.; Kohlstedt, H.; Park, N.; Stephenson, G. Ferroelectric thin films: Review of materials, properties, and applications. *J Appl Phys* **2006**, *100*.
4. Zhang, D.; Wu, H.; Bowen, C.R.; Yang, Y. Recent advances in pyroelectric materials and applications. *Small* **2021**, *17*, 2103960.
5. Chen, X.; Xu, S.; Yao, N.; Shi, Y. 1.6 V Nanogenerator for Mechanical Energy Harvesting Using PZT Nanofibers. *Nano Letters* **2010**, *10*, 2133-2137.
6. Shi, Q.; Wang, T.; Lee, C. MEMS based broadband piezoelectric ultrasonic energy harvester (PUEH) for enabling self-powered implantable biomedical devices. *Scientific reports* **2016**, *6*, 24946.
7. Todaro, M.T.; Guido, F.; Mastronardi, V.; Desmaele, D.; Epifani, G.; Algieri, L.; De Vittorio, M. Piezoelectric MEMS vibrational energy harvesters: Advances and outlook. *Microelectronic Engineering* **2017**, *183*, 23-36.
8. Meng, C.; Thrane, P.C.; Ding, F.; Bozhevolnyi, S.I. Full-range birefringence control with piezoelectric MEMS-based metasurfaces. *Nat Commun* **2022**, *13*, 2071.
9. Scott, J. Applications of modern ferroelectrics. *Science* **2007**, *315*, 954-959.
10. Scott, J.F. Applications of magnetoelectrics. *J Mater Chem* **2012**, *22*, 4567-4574.
11. Martin, L.W.; Rappe, A.M. Thin-film ferroelectric materials and their applications. *Nature Reviews Materials* **2016**, *2*, 1-14.
12. Mikolajick, T.; Schroeder, U.; Slesazeck, S. The past, the present, and the future of ferroelectric memories. *Ieee T Electron Dev* **2020**, *67*, 1434-1443.
13. Lim, H.E.; Nakanishi, Y.; Liu, Z.; Pu, J.; Maruyama, M.; Endo, T.; Ando, C.; Shimizu, H.; Yanagi, K.; Okada, S. Wafer-Scale Growth of One-Dimensional Transition-Metal Telluride Nanowires. *Nano Letters* **2020**, *21*, 243-249.
14. Varghese, J.; O'Regan, C.; Deepak, N.; Whatmore, R.W.; Holmes, J.D. Surface roughness assisted growth of vertically oriented ferroelectric SbSI nanorods. *Chem Mater* **2012**, *24*, 3279-3284.
15. Ji, S.; Liu, H.; Sang, Y.; Liu, W.; Yu, G.; Leng, Y. Synthesis, structure, and piezoelectric properties of ferroelectric and antiferroelectric NaNbO 3 nanostructures. *Crystengcomm* **2014**, *16*, 7598-7604.
16. Buscaglia, M.T.; Sennour, M.; Buscaglia, V.; Bottino, C.; Kalyani, V.; Nanni, P. Formation of Bi4Ti3O12 one-dimensional structures by solid-state reactive diffusion. From core− shell templates to nanorods and nanotubes. *Cryst Growth Des* **2011**, *11*, 1394-1401.

17. Yang, P.; Ding, Y.; Lin, Z.; Chen, Z.; Li, Y.; Qiang, P.; Ebrahimi, M.; Mai, W.; Wong, C.P.; Wang, Z.L. Low-cost high-performance solid-state asymmetric supercapacitors based on MnO2 nanowires and Fe2O3 nanotubes. *Nano letters* **2014**, *14*, 731-736.
18. Kim, J.; Yang, S.A.; Choi, Y.C.; Han, J.K.; Jeong, K.O.; Yun, Y.J.; Kim, D.J.; Yang, S.M.; Yoon, D.; Cheong, H. Ferroelectricity in highly ordered arrays of ultra-thin-walled Pb (Zr, Ti) O3 nanotubes composed of nanometer-sized perovskite crystallites. *Nano Letters* **2008**, *8*, 1813-1818.
19. Wang, W.; Ke, H.; Rao, J.-C.; Feng, M.; Zhou, Y. Sol–Gel synthesis of SrBi2Ta2O9 nanowires. *J Alloy Compd* **2010**, *504*, 367-370.
20. Karvounis, A.; Timpu, F.; Vogler-Neuling, V.V.; Savo, R.; Grange, R. Barium titanate nanostructures and thin films for photonics. *Adv Opt Mater* **2020**, *8*, 2001249.
21. Isakov, D.V.; de Matos Gomes, E.; Vieira, L.G.; Dekola, T.; Belsley, M.S.; Almeida, B.G. Oriented single-crystal-like molecular arrangement of optically nonlinear 2-methyl-4-nitroaniline in electrospun nanofibers. *Acs Nano* **2011**, *5*, 73-78.
22. Wendorff, J.H.; Agarwal, S.; Greiner, A. *Electrospinning: materials, processing, and applications*; John Wiley & Sons: 2012.
23. Starr, J.D.; Andrew, J.S. Janus-type bi-phasic functional nanofibers. *Chem Commun* **2013**, *49*, 4151-4153.
24. Isakov, D.; Gomes, E.D.; Almeida, B.; Kholkin, A.L.; Zelenovskiy, P.; Neradovskiy, M.; Shur, V.Y. Energy harvesting from nanofibers of hybrid organic ferroelectric dabcoHReO(4). *Appl Phys Lett* **2014**, *104*, 4.
25. Sun, B.; Long, Y.Z.; Zhang, H.D.; Li, M.M.; Duvail, J.L.; Jiang, X.Y.; Yin, H.L. Advances in three-dimensional nanofibrous macrostructures via electrospinning. *Prog Polym Sci* **2014**, *39*, 862-890.
26. Bernardo, C.R.; Baptista, R.M.F.; de Matos Gomes, E.; Lopes, P.E.; Raposo, M.M.M.; Costa, S.P.G.; Belsley, M.S. Anisotropic PCL nanofibers embedded with nonlinear nanocrystals as strong generators of polarized second harmonic light and piezoelectric currents. *Nanoscale Advances* **2020**, *2*, 1206-1213.
27. Laramée, A.W.; Lanthier, C.; Pellerin, C. Electrospinning of Highly Crystalline Polymers for Strongly Oriented Fibers. *ACS Applied Polymer Materials* **2020**, *2*, 5025-5032.
28. Greiner, A.; Wendorff, J.H. Electrospinning: A Fascinating Method for the Preparation of Ultrathin Fibers. *Angewandte Chemie International Edition* **2007**, *46*, 5670-5703.
29. Ramakrishna, S.; Fujihara, K.; Teo, W.-E.; Yong, T.; Ma, Z.; Ramaseshan, R. Electrospun nanofibers: solving global issues. *Materials Today* **2006**, *9*, 40-50.
30. Ramakrishna, S.; Fujihara, K.; Teo, W.-E.; Lim, T.-C.; Ma, Z. *An Introduction to Electrospinning and Nanofibers*; WORLD SCIENTIFIC: 2005; p. 396.
31. Li, D.; Xia, Y. Electrospinning of Nanofibers: Reinventing the Wheel? *Adv Mater* **2004**, *16*, 1151-1170.
32. Huang, Z.-M.; Zhang, Y.Z.; Kotaki, M.; Ramakrishna, S. A review on polymer nanofibers by electrospinning and their applications in nanocomposites. *Composites Science and Technology* **2003**, *63*, 2223-2253.
33. Prateek; Thakur, V.K.; Gupta, R.K. Recent progress on ferroelectric polymer-based nanocomposites for high energy density capacitors: synthesis, dielectric properties, and future aspects. *Chemical reviews* **2016**, *116*, 4260-4317.
34. Habib, M.; Lantgios, I.; Hornbostel, K. A review of ceramic, polymer and composite piezoelectric materials. *Journal of Physics D: Applied Physics* **2022**, *55*, 423002.
35. Wang, X.; Fan, J.; Manikandan, M.; Zhang, B.; Guo, J.; Chen, J.; Yang, F.; Zheng, M.; Zhang, H.; Hou, M. Recent advances in composite films of lead-free ferroelectric ceramics and poly (vinylidene fluoride)(PVDF) for energy storage capacitor: a review. *Journal of Materials Science* **2023**, *58*, 124-143.
36. Pal, S.; Sarath, N.; Priya, K.S.; Murugavel, P. A review on ferroelectric systems for next generation photovoltaic applications. *Journal of Physics D: Applied Physics* **2022**, *55*, 283001.
37. Jayakrishnan, A.R.; Kumar, A.; Druvakumar, S.; John, R.; Sudeesh, M.; Puli, V.S.; Silva, J.P.; Gomes, M.J.; Sekhar, K.C. Inorganic ferroelectric thin films and their composites for flexible electronic and energy device applications: current progress and perspectives. *Journal of Materials Chemistry C* **2023**, *11*, 827-858.
38. Bakhtiar, S.U.H.; abbas Hussain, S.; Ali, S.; Ismail, A.; Zada, A.; Sattar, H.; Raziq, F.; Zahid, M.; Al-Fatesh, A.S.; Dong, W. Innovative Perspectives on Porous Ferroelectric Ceramics and their Composites: Charting New Frontiers in Energy Applications. *Materials Today Communications* **2024**, 108388.

39. Starr, J.D.; Andrew, J.S. A route to synthesize multifunctional tri-phasic nanofibers. *Journal of Materials Chemistry C* **2013**, *1*, 2529-2533.
40. Koka, A.; Sodano, H.A. High-sensitivity accelerometer composed of ultra-long vertically aligned barium titanate nanowire arrays. *Nat Commun* **2013**, *4*, 2682.
41. Jiang, Y.; Zhou, M.; Shen, Z.; Zhang, X.; Pan, H.; Lin, Y.-H. Ferroelectric polymers and their nanocomposites for dielectric energy storage applications. *Apl Mater* **2021**, *9*, 020905.
42. Kim, H.-Y.; Lee, M.; Park, K.J.; Kim, S.; Mahadevan, L. Nanopottery: Coiling of Electrospun Polymer Nanofibers. *Nano Letters* **2010**, *10*, 2138-2140.
43. Luo, G.; Teh, K.S.; Liu, Y.; Zang, X.; Wen, Z.; Lin, L. Direct-Write, Self-Aligned Electrospinning on Paper for Controllable Fabrication of Three-Dimensional Structures. *Acs Appl Mater Inter* **2015**, *7*, 27765-27770.
44. Cai, M.Q.; Zheng, Y.; Wang, B.; Yang, G.W. Nanosize confinement induced enhancement of spontaneous polarization in a ferroelectric nanowire. *Appl Phys Lett* **2009**, *95*, 232901.
45. Wang, Z.; Hu, J.; Suryavanshi, A.P.; Yum, K.; Yu, M.-F. Voltage Generation from Individual BaTiO3 Nanowires under Periodic Tensile Mechanical Load. *Nano Letters* **2007**, *7*, 2966-2969.
46. Wang, W.; Li, J.; Liu, H.; Ge, S. Advancing Versatile Ferroelectric Materials Toward Biomedical Applications. *Adv Sci* **2021**, *8*, 2003074.
47. Koka, A.; Zhou, Z.; Sodano, H.A. Vertically aligned BaTiO3 nanowire arrays for energy harvesting. *Energy & Environmental Science* **2014**, *7*, 288-296.
48. Zhou, Z.; Tang, H.; Sodano, H.A. Vertically Aligned Arrays of BaTiO3 Nanowires. *Acs Appl Mater Inter* **2013**, *5*, 11894-11899.
49. Baji, A.; Mai, Y.-W.; Li, Q.; Liu, Y. Electrospinning induced ferroelectricity in poly(vinylidene fluoride) fibers. *Nanoscale* **2011**, *3*, 3068-3071.
50. Noyori, M.; Neo, Y.; Mimura, H. Single-crystalline poly(vinylidene fluoride–trifluoroethylene) nanofiber webs fabricated by electrospinning. *Jpn J Appl Phys* **2015**, *54*, 021601.
51. Xin, Y.; Zhu, J.; Sun, H.; Xu, Y.; Liu, T.; Qian, C. A brief review on piezoelectric PVDF nanofibers prepared by electrospinning. *Ferroelectrics* **2018**, *526*, 140-151.
52. He, Z.; Rault, F.; Lewandowski, M.; Mohsenzadeh, E.; Salaün, F. Electrospun PVDF nanofibers for piezoelectric applications: A review of the influence of electrospinning parameters on the β phase and crystallinity enhancement. *Polymers* **2021**, *13*, 174.
53. Liu, Y.; Zhang, Y.; Chow, M.-J.; Chen, Q.N.; Li, J. Biological ferroelectricity uncovered in aortic walls by piezoresponse force microscopy. *Phys Rev Lett* **2012**, *108*, 078103.
54. Liu, Y.; Wang, Y.; Chow, M.-J.; Chen, N.Q.; Ma, F.; Zhang, Y.; Li, J. Glucose suppresses biological ferroelectricity in aortic elastin. *Phys Rev Lett* **2013**, *110*, 168101.
55. Coste, B.; Xiao, B.; Santos, J.S.; Syeda, R.; Grandl, J.; Spencer, K.S.; Kim, S.E.; Schmidt, M.; Mathur, J.; Dubin, A.E. Piezo proteins are pore-forming subunits of mechanically activated channels. *Nature* **2012**, *483*, 176-181.
56. Liu, Y.; Cai, H.-L.; Zelisko, M.; Wang, Y.; Sun, J.; Yan, F.; Ma, F.; Wang, P.; Chen, Q.N.; Zheng, H. Ferroelectric switching of elastin. *Proceedings of the National Academy of Sciences* **2014**, *111*, E2780-E2786.
57. Balizer, E.; Fedderly, J.; Haught, D.; Dickens, B.; Dereggi, A. FTIR and X-ray study of polymorphs of nylon 11 and relation to ferroelectricity. *Journal of Polymer Science Part B: Polymer Physics* **1994**, *32*, 365-369.
58. Itoh, T.; Tanaka, T.; Hashimoto, M.; Takashi Konishi, T.K. Ferroelectric Hysteresis Behavior and Structural Property of Even-Numbered Nylon Film. *Jpn J Appl Phys* **1995**, *34*, 6164.
59. Capsal, J.-F.; Dantras, E.; Dandurand, J.; Lacabanne, C. Dielectric relaxations and ferroelectric behaviour of even–odd polyamide PA 6,9. *Polymer* **2010**, *51*, 4606-4610.
60. Murata, Y.; Tsunashima, K.; Umemura, J.; Koizumi, N. Ferroelectric properties of polyamides consisting of hepta- and nonamethylenediamines. *IEEE Transactions on Dielectrics and Electrical Insulation* **1998**, *5*, 96-102.
61. Wu, J.; Fu, Y.; Hu, G.-H.; Wang, S.; Xiong, C. Effect of Stretching on Crystalline Structure, Ferroelectric and Piezoelectric Properties of Solution-Cast Nylon-11 Films. *Polymers* **2021**, *13*, 2037.
62. Eom, K.; Na, S.; Kim, J.-K.; Ko, H.; Jin, J.; Kang, S.J. Engineering crystal phase of Nylon-11 films for ferroelectric device and piezoelectric sensor. *Nano Energy* **2021**, *88*, 106244.

63. Prasad, G.; Graham, S.A.; Yu, J.S.; Kim, H.; Lee, D.-W. Investigated a PLL surface-modified Nylon 11 electrospun as a highly tribo-positive frictional layer to enhance output performance of triboelectric nanogenerators and self-powered wearable sensors. *Nano Energy* **2023**, *108*, 108178.
64. Tu, N.D.K.; Park, J.; Na, S.; Kim, K.M.; Kwon, T.-H.; Ko, H.; Kang, S.J. Co-solvent induced piezoelectric γ-phase nylon-11 separator for sodium metal battery. *Nano Energy* **2020**, *70*, 104501.
65. Kim, D.K.; Hwang, M.; Lagerwall, J.P.F. Liquid crystal functionalization of electrospun polymer fibers. *Journal of Polymer Science Part B: Polymer Physics* **2013**, *51*, 855-867.
66. Zhou, L.; Liu, S.; Miao, X.; Xie, P.; Sun, N.; Xu, Z.; Zhong, T.; Zhang, L.; Shen, Y. Advancements and Applications of Liquid Crystal/Polymer Composite Films. *ACS Materials Letters* **2023**, *5*, 2760-2775.
67. Bertocchi, M.J.; Ratchford, D.C.; Casalini, R.; Wynne, J.H.; Lundin, J.G. Electrospun polymer fibers containing a liquid crystal core: insights into semiflexible confinement. *The Journal of Physical Chemistry C* **2018**, *122*, 16964-16973.
68. Nguyen, J.; Stwodah, R.M.; Vasey, C.L.; Rabatin, B.E.; Atherton, B.; D'Angelo, P.A.; Swana, K.W.; Tang, C. Thermochromic fibers via electrospinning. *Polymers* **2020**, *12*, 842.
69. Lagerwall, J.P.; McCann, J.T.; Formo, E.; Scalia, G.; Xia, Y. Coaxial electrospinning of microfibres with liquid crystal in the core. *Chem Commun* **2008**, 5420-5422.
70. Reyes, C.G.; Sharma, A.; Lagerwall, J.P. Non-electronic gas sensors from electrospun mats of liquid crystal core fibres for detecting volatile organic compounds at room temperature. *Liq Cryst* **2016**, *43*, 1986-2001.
71. Williams, M.W.; Wimberly, J.A.; Stwodah, R.M.; Nguyen, J.; D'Angelo, P.A.; Tang, C. Temperature-Responsive Structurally Colored Fibers via Blend Electrospinning. *ACS Applied Polymer Materials* **2023**, *5*, 3065-3078.
72. Sharma, A.; Lagerwall, J.P. Electrospun composite liquid crystal elastomer fibers. *Materials* **2018**, *11*, 393.
73. Kularatne, R.S.; Kim, H.; Boothby, J.M.; Ware, T.H. Liquid crystal elastomer actuators: Synthesis, alignment, and applications. *Journal of Polymer Science Part B: Polymer Physics* **2017**, *55*, 395-411.
74. Liu, Y.; Luo, H.; Gao, Z.; Xie, H.; Guo, R.; Wang, F.; Zhou, X.; Cao, J.; Zhang, D. Electrospinning Synthesis of Na0. 5Bi0. 5TiO3 Nanofibers for Dielectric Capacitors in Energy Storage Application. *Nanomaterials* **2022**, *12*, 906.
75. Yuh, J.; Nino, J.C.; Sigmund, W.M. Synthesis of barium titanate (BaTiO3) nanofibers via electrospinning. *Mater Lett* **2005**, *59*, 3645-3647.
76. Sá, P.; Barbosa, J.; Bdikin, I.; Almeida, B.; Rolo, A.G.; Gomes, E.d.M.; Belsley, M.; Kholkin, A.L.; Isakov, D. Ferroelectric characterization of aligned barium titanate nanofibres. *Journal of Physics D: Applied Physics* **2013**, *46*, 105304.
77. Ganeshkumar, R.; Sopiha, K.V.; Wu, P.; Cheah, C.W.; Zhao, R. Ferroelectric KNbO3nanofibers: synthesis, characterization and their application as a humidity nanosensor. *Nanotechnology* **2016**, *27*, 395607.
78. Jalalian, A.; Grishin, A.M. Biocompatible ferroelectric (Na,K)NbO3 nanofibers. *Appl Phys Lett* **2012**, *100*, 012904.
79. Chen, X.; Xu, S.; Yao, N.; Xu, W.; Shi, Y. Potential measurement from a single lead ziroconate titanate nanofiber using a nanomanipulator. *Appl Phys Lett* **2009**, *94*, 253113.
80. Zhu, R.; Wang, Z.; Cheng, Z.; Kimura, H. 10 - Ferroelectric nanofibers and their application in energy harvesting. In *Nanoscale Ferroelectric-Multiferroic Materials for Energy Harvesting Applications*, Kimura, H., Cheng, Z., Jia, T., Eds.; Elsevier: 2019; pp. 181-194.
81. Yan, J.; Jeong, Y.G. High performance flexible piezoelectric nanogenerators based on BaTiO3 nanofibers in different alignment modes. *Acs Appl Mater Inter* **2016**, *8*, 15700-15709.
82. Zhao, Y.; Fan, H.; Liu, G.; Liu, Z.; Ren, X. Ferroelectric, piezoelectric properties and magnetoelectric coupling behavior in aurivillius Bi5Ti3FeO15 multiferroic nanofibers by electrospinning. *J Alloy Compd* **2016**, *675*, 441-447.
83. Li, B.; Wang, C.; Liu, W.; Zhong, Y.; An, R. Synthesis of Co-doped barium strontium titanate nanofibers by sol–gel/electrospinning process. *Mater Lett* **2012**, *75*, 207-210.
84. Wang, Y.; Santiago-Avilés, J.J. A Review on Synthesis and Characterization of Lead Zirconate Titanate Nanofibers through Electrospinning. *Integrated Ferroelectrics* **2011**, *126*, 60-76.

 doi:10.20944/preprints202501.2184.v1

85. Yousefi, F.; Esfahani, H. Role of Nb5+-Nd3+ co-dopant in morphotropic boundary of electrospun PZT nanoneedles: Study on dielectric and piezoelectric sensitivity. *J Alloy Compd* **2023**, *966*, 171531.
86. Gu, L.; Cui, N.; Cheng, L.; Xu, Q.; Bai, S.; Yuan, M.; Wu, W.; Liu, J.; Zhao, Y.; Ma, F.; et al. Flexible Fiber Nanogenerator with 209 V Output Voltage Directly Powers a Light-Emitting Diode. *Nano Letters* **2013**, *13*, 91-94.
87. Wu, W.; Bai, S.; Yuan, M.; Qin, Y.; Wang, Z.L.; Jing, T. Lead Zirconate Titanate Nanowire Textile Nanogenerator for Wearable Energy-Harvesting and Self-Powered Devices. *Acs Nano* **2012**, *6*, 6231-6235.
88. Xia, S.; Wei, C.; Zhai, Y.; Ding, B.; Yu, J.; Yan, J. Ultrasonic cavitation enhanced photocatalytic CO2 reduction by superior flexible black BaTiO3 nanofibers. *Chemical Engineering Journal* **2023**, *475*, 146516.
89. Maensiri, S.; Nuansing, W.; Klinkaewnarong, J.; Laokul, P.; Khemprasit, J. Nanofibers of barium strontium titanate (BST) by sol–gel processing and electrospinning. *J Colloid Interf Sci* **2006**, *297*, 578-583.
90. Pan, Z.B.; Yao, L.M.; Zhai, J.W.; Liu, S.H.; Yang, K.; Wang, H.T.; Liu, J.H. Fast discharge and high energy density of nanocomposite capacitors using Ba0.6Sr0.4TiO3 nanofibers. *Ceramics International* **2016**, *42*, 14667-14674.
91. Maldonado-Orozco, M.C.; Ochoa-Lara, M.T.; Sosa-Márquez, J.E.; Olive-Méndez, S.F.; Espinosa-Magaña, F. Synthesis and characterization of electrospun LiNbO3 nanofibers. *Ceramics International* **2015**, *41*, 14886-14889.
92. Maldonado-Orozco, M.C.; Ochoa-Lara, M.T.; Sosa-Márquez, J.E.; Olive-Méndez, S.F.; Pizá-Ruiz, P.; Quintanar-Sierra, J.J.C.; Espinosa-Magaña, F. Characterization of Mn-doped electrospun LiNbO3 nanofibers by Raman spectroscopy. *Materials Characterization* **2017**, *127*, 209-213.
93. Zhou, B.; Li, C.; Zhou, Y.; Liu, Z.; Gao, X.; Wang, X.; Jiang, L.; Tian, M.; Zhou, F.-L.; Jerrams, S.; et al. A flexible dual-mode pressure sensor with ultra-high sensitivity based on BTO@MWCNTs core-shell nanofibers. *Composites Science and Technology* **2022**, *224*, 109478.
94. Ichangi, A.; Lê, K.; Queraltó, A.; Grosch, M.; Weißing, R.; Ünlü, F.; Chijioke, A.K.; Verma, A.; Fischer, T.; Surmenev, R.; et al. Electrospun BiFeO3 Nanofibers for Vibrational Energy Harvesting Application. *Adv Eng Mater* **2022**, *24*, 2101394.
95. Fei, L.; Hu, Y.; Li, X.; Song, R.; Sun, L.; Huang, H.; Gu, H.; Chan, H.L.W.; Wang, Y. Electrospun Bismuth Ferrite Nanofibers for Potential Applications in Ferroelectric Photovoltaic Devices. *Acs Appl Mater Inter* **2015**, *7*, 3665-3670.
96. Fourmont, P.; Nechache, R.; Cloutier, S.G. Reusable BiFeO3 Nanofiber-Based Membranes for Photo-activated Organic Pollutant Removal with Negligible Colloidal Release. *ACS Applied Nano Materials* **2021**, *4*, 12261-12269.
97. Sá, P.; Bdikin, I.; Almeida, B.; Rolo, A.G.; Isakov, D. Production and PFM Characterization of Barium Titanate Nanofibers. *Ferroelectrics* **2012**, *429*, 48-55.
98. Wei, Y.; Song, Y.; Deng, X.; Han, B.; Zhang, X.; Shen, Y.; Lin, Y. Dielectric and ferroelectric properties of BaTiO3 nanofibers prepared via electrospinning. *Journal of Materials Science & Technology* **2014**, *30*, 743-747.
99. Yan, J.; Han, Y.; Xia, S.; Wang, X.; Zhang, Y.; Yu, J.; Ding, B. Polymer template synthesis of flexible BaTiO3 crystal nanofibers. *Adv Funct Mater* **2019**, *29*, 1907919.
100. Tang, M.; Shu, W.; Yang, F.; Zhang, J.; Dong, G.; Hou, J. The fabrication of La-substituted bismuth titanate nanofibers by electrospinning. *Nanotechnology* **2009**, *20*, 385602.
101. Choi, S.; Park, J.; Kang, J.; Koh, S.W.; Kang, Y.C. Synthesis and characterization of lead zirconate titanate nanofibers obtained by electrospinning. *B Kor Chem Soc* **2015**, *36*, 1594-1598.
102. Spaldin, N.A.; Ramesh, R. Advances in magnetoelectric multiferroics. *Nat Mater* **2019**, *18*, 203-212.
103. Leung, C.M.; Li, J.; Viehland, D.; Zhuang, X. A review on applications of magnetoelectric composites: From heterostructural uncooled magnetic sensors, energy harvesters to highly efficient power converters. *Journal of Physics D: Applied Physics* **2018**, *51*, 263002.
104. Hu, J.M.; Chen, L.Q.; Nan, C.W. Multiferroic heterostructures integrating ferroelectric and magnetic materials. *Adv Mater* **2016**, *28*, 15-39.
105. Hu, J.-M.; Nan, C.-W.; Chen, L.-Q. Perspective: voltage control of magnetization in multiferroic heterostructures. *National Science Review* **2019**, *6*, 621-624.

106. Lin, H.; Gao, Y.; Wang, X.; Nan, T.; Liu, M.; Lou, J.; Yang, G.; Zhou, Z.; Yang, X.; Wu, J. Integrated magnetics and multiferroics for compact and power-efficient sensing, memory, power, RF, and microwave electronics. *Ieee T Magn* **2016**, *52*, 1-8.
107. Manipatruni, S.; Nikonov, D.E.; Young, I.A. Beyond CMOS computing with spin and polarization. *Nature Physics* **2018**, *14*, 338-343.
108. Bichurin, M.; Petrov, R.; Sokolov, O.; Leontiev, V.; Kuts, V.; Kiselev, D.; Wang, Y. Magnetoelectric Magnetic Field Sensors: A Review. *Sensors-Basel* **2021**, *21*, 6232.
109. Zuo, S.; Schmalz, J.; Özden, M.Ö.; Gerken, M.; Su, J.; Niekiel, F.; Lofink, F.; Nazarpour, K.; Heidari, H. Ultrasensitive Magnetoelectric Sensing System for Pico-Tesla MagnetoMyoGraphy. *IEEE Transactions on Biomedical Circuits and Systems* **2020**, *14*, 971-984.
110. Lorenz, M.; Lazenka, V.; Schwinkendorf, P.; Bern, F.; Ziese, M.; Modarresi, H.; Volodin, A.; Van Bael, M.J.; Temst, K.; Vantomme, A. Multiferroic BaTiO3–BiFeO3 composite thin films and multilayers: strain engineering and magnetoelectric coupling. *Journal of Physics D: Applied Physics* **2014**, *47*, 135303.
111. Pradhan, D.K.; Kumari, S.; Rack, P.D. Magnetoelectric composites: applications, coupling mechanisms, and future directions. *Nanomaterials* **2020**, *10*, 2072.
112. Andrew, J.S.; Starr, J.D.; Budi, M.A. Prospects for nanostructured multiferroic composite materials. *Scripta Materialia* **2014**, *74*, 38-43.
113. Zhang, C.; Chen, W.; Xie, S.; Yang, J.; Li, J. The magnetoelectric effects in multiferroic composite nanofibers. *Appl Phys Lett* **2009**, *94*.
114. Xie, S.; Ma, F.; Liu, Y.; Li, J. Multiferroic CoFe 2 O 4–Pb (Zr 0.52 Ti 0.48) O 3 core-shell nanofibers and their magnetoelectric coupling. *Nanoscale* **2011**, *3*, 3152-3158.
115. Liu, Y.; Sreenivasulu, G.; Zhou, P.; Fu, J.; Filippov, D.; Zhang, W.; Zhou, T.; Zhang, T.; Shah, P.; Page, M.R.; et al. Converse magneto-electric effects in a core–shell multiferroic nanofiber by electric field tuning of ferromagnetic resonance. *Scientific Reports* **2020**, *10*, 20170.
116. Sreenivasulu, G.; Popov, M.; Zhang, R.; Sharma, K.; Janes, C.; Mukundan, A.; Srinivasan, G. Magnetic field assisted self-assembly of ferrite-ferroelectric core-shell nanofibers and studies on magneto-electric interactions. *Appl Phys Lett* **2014**, *104*.
117. Yadav, S.K.; Hemalatha, J. Electrospinning and characterization of magnetoelectric NdFeO3–PbZr0. 52Ti0. 48O3 core–shell nanofibers. *Ceramics International* **2022**, *48*, 18415-18424.
118. Zhu, Q.; Xie, Y.; Zhang, J.; Liu, Y.; Zhan, Q.; Miao, H.; Xie, S. Multiferroic CoFe 2 O 4–BiFeO 3 core–shell nanofibers and their nanoscale magnetoelectric coupling. *J Mater Res* **2014**, *29*, 657-664.
119. Li, Z.; Dai, J.; Huang, D.; Wen, X. Tuning the ferromagnetic and ferroelectric properties of BiFeO3 multiferroic nanofibers by Co/Ni spinel ferrites. *J Alloy Compd* **2022**, *907*, 164386.
120. Sreenivasulu, G.; Zhang, J.; Zhang, R.; Popov, M.; Petrov, V.; Srinivasan, G. Multiferroic core-shell nanofibers, assembly in a magnetic field, and studies on magneto-electric interactions. *Materials* **2017**, *11*, 18.
121. Molavi, A.M.; Alizadeh, P. Electrospinning of multiferroic CoFe2O4@ Ba (Zr0. 2Ti0. 8) O3–0.5 (Ba0. 7Ca0. 3) TiO3 nano-structured fibers via two different routes. *Materials Characterization* **2021**, *172*, 110880.
122. Yadav, S.K.; Hemalatha, J. Direct magnetoelectric and magnetodielectric studies of electrospun Ba2Ni2Fe12O22–Pb(Zr0.52Ti0.48)O3 core–shell nanofibers. *J Magn Magn Mater* **2022**, *564*, 170174.
123. Hadouch, Y.; Mezzane, D.; Amjoud, M.b.; Laguta, V.; Hoummada, K.; Dolocan, V.O.; Jouiad, M.; Lahcini, M.; Uršič, H.; Fišinger, V.; et al. Multiferroic CoFe2O4–Ba0.95Ca0.05Ti0.89Sn0.11O3 Core–Shell Nanofibers for Magnetic Field Sensor Applications. *ACS Applied Nano Materials* **2023**, *6*, 10236-10245.
124. Li, B.; Wang, C.; Zhang, W.; Hang, C.; Fei, J.; Wang, H. Fabrication of multiferroic Ba0. 7Sr0. 3TiO3–Ni0. 8Zn0. 2Fe2O4 composite nanofibers by electrospinning. *Mater Lett* **2013**, *91*, 55-58.
125. Fu, B.; Lu, R.; Gao, K.; Yang, Y.; Wang, Y. Magnetoelectric coupling in multiferroic BaTiO3-CoFe2O4 composite nanofibers via electrospinning. *Europhysics Letters* **2015**, *111*, 17007.
126. Xie, S.; Li, J.; Qiao, Y.; Liu, Y.; Lan, L.; Zhou, Y.; Tan, S. Multiferroic CoFe2O4–Pb (Zr0. 52Ti0. 48) O3 nanofibers by electrospinning. *Appl Phys Lett* **2008**, *92*.
127. Zhu, Q.; Pan, K.; Xie, S.; Liu, Y.; Li, J. Nanomechanics of multiferroic composite nanofibers via local excitation piezoresponse force microscopy. *Journal of the Mechanics and Physics of Solids* **2019**, *126*, 76-86.

128. Xie, S.; Li, J.; Liu, Y.; Lan, L.; Jin, G.; Zhou, Y. Electrospinning and multiferroic properties of NiFe2O4–Pb (Zr0. 52Ti0. 48) O3 composite nanofibers. *J Appl Phys* **2008**, *104*.
129. Hadouch, Y.; Abdallah, N.; Mezzane, D.; Amjoud, M.b.; Dolocan, V.; Hoummada, K.; Novak, N.; Razumnaya, A.; Rozic, B.; Fisinger, V. Multiferroic properties of electrospun CoFe2O4–(Ba0. 95Ca0. 05)(Ti0. 89Sn0. 11) O3 nanocomposites for magnetoelectric and magnetic field sensing applications. *Journal of Materials Science: Materials in Electronics* **2024**, *35*, 1794.
130. An, F.; Zhong, G.; Zhu, Q.; Huang, Y.; Yang, Y.; Xie, S. Synthesis and mechanical properties characterization of multiferroic BiFeO3-CoFe2O4 composite nanofibers. *Ceramics International* **2018**, *44*, 11617-11621.
131. Liu, Z.; Sun, D.D.; Guo, P.; Leckie, J.O. An efficient bicomponent TiO2/SnO2 nanofiber photocatalyst fabricated by electrospinning with a side-by-side dual spinneret method. *Nano letters* **2007**, *7*, 1081-1085.
132. Starr, J.D.; Budi, M.A.; Andrew, J.S. Processing-Property Relationships in Electrospun Janus-Type Biphasic Ceramic Nanofibers. *J Am Ceram Soc* **2015**, *98*, 12-19.
133. Dolbashian, C.; Chavez, B.; Bauer, M.; Budi, M.; Andrew, J.S.; Crawford, T.M. Magnetic properties of aligned multiferroic Janus nanofiber agglomerates measured with the scattered magneto-optical Kerr effect. *Journal of Physics D: Applied Physics* **2020**, *53*, 195002.
134. Arash, S.; Kharal, G.; Chavez, B.L.; Ferson, N.D.; Mills, S.C.; Andrew, J.S.; Crawford, T.M.; Wu, Y. Multiferroicity and Semi-Cylindrical Alignment in Janus Nanofiber Aggregates. *Adv Funct Mater* **2024**, 2412690.
135. Chavez, B.L.; Sosnowski, K.C.; Bauer, M.J.; Budi, M.A.; Andrew, J.S.; Crawford, T.M. Toward nanoscale multiferroic devices: Magnetic field-directed self-assembly and chaining in Janus nanofibers. *Aip Adv* **2018**, *8*.
136. Isakov, D.V.; Gomes, E.d.M.; Almeida, B.G.; Bdikin, I.K.; Martins, A.M.; Kholkin, A.L. Piezoresponse force microscopy studies of the triglycine sulfate-based nanofibers. *J Appl Phys* **2010**, *108*, 042011.
137. Isakov, D.; Gomes, E.d.M.; Bdikin, I.; Almeida, B.; Belsley, M.; Costa, M.; Rodrigues, V.; Heredia, A. Production of Polar β-Glycine Nanofibers with Enhanced Nonlinear Optical and Piezoelectric Properties. *Cryst Growth Des* **2011**, *11*, 4288-4291.
138. Isakov, D.; Martins, A.M.; Gomes, E.d.M.; Bdikin, I.; Guimarães, A.; Dekola, T.; Almeida, B.; Neves, N.M.; Reis, R.L.; Macedo, F. Synthesis of polymer-based triglycine sulfate nanofibres by electrospinning. *Journal of Physics D: Applied Physics* **2009**, *42*, 205403.
139. Baptista, R.M.F.; Isakov, D.; Raposo, M.M.M.; Belsley, M.; Bdikin, I.; Kholkin, A.L.; Costa, S.P.G.; de Matos Gomes, E. Ferroelectric nanofibers with an embedded optically nonlinear benzothiazole derivative. *J Nanopart Res* **2014**, *16*, 2502.
140. Nye, J.F. *Physical properties of crystals : their representation by tensors and matrices*, Repr. paperback ed. ed.; Oxford : Clarendon press: 2004.
141. Baptista, R.M.F.; Moreira, G.; Silva, B.; Oliveira, J.; Almeida, B.; Castro, C.; Rodrigues, P.V.; Machado, A.; Belsley, M.; de Matos Gomes, E. Lead-Free MDABCO-NH4I3 Perovskite Crystals Embedded in Electrospun Nanofibers. *Materials* **2022**, *15*, 8397.
142. Chemla, D.S. *Nonlinear Optical Properties of Organic Molecules and Crystals*; Academic Press: New York, 1987.
143. Isakov, D.; de Matos Gomes, E.; Belsley, M.; Almeida, B.; Martins, A.; Neves, N.; Reis, R. High nonlinear optical anisotropy of urea nanofibers. *EPL (Europhysics Letters)* **2010**, *91*, 28007.
144. Kongkhlang, T.; Tashiro, K.; Kotaki, M.; Chirachanchai, S. Electrospinning as a New Technique To Control the Crystal Morphology and Molecular Orientation of Polyoxymethylene Nanofibers. *J Am Chem Soc* **2008**, *130*, 15460-15466.
145. Isakov, D.; Gomes, E.D.; Belsley, M.S.; Almeida, B.; Cerca, N. Strong enhancement of second harmonic generation in 2-methyl-4-nitroaniline nanofibers. *Nanoscale* **2012**, *4*, 4978-4982.
146. Woodford, J.; Pauley, M.; Wang, C. Solvent dependence of the first molecular hyperpolarizability of p-nitroaniline revisited. *The Journal of Physical Chemistry A* **1997**, *101*, 1989-1992.
147. Karna, S.P.; Prasad, P.N.; Dupuis, M. Nonlinear optical properties of p-nitroaniline: An ab initio time-dependent coupled perturbed Hartree–Fock study. *The Journal of chemical physics* **1991**, *94*, 1171-1181.
148. Champagne, B. Vibrational polarizability and hyperpolarizability of p-nitroaniline. *Chem Phys Lett* **1996**, *261*, 57-65.

 doi:10.20944/preprints202501.2184.v1

149. Trueblood, K.N.; Goldish, E.; Donohue, J. A three-dimensional refinement of the crystal structure of 4-nitroaniline. *Acta Crystallographica* **1961**, *14*, 1009-1017.
150. Isakov, D.V.; Belsley, M.S.; de Matos Gomes, E.; Goncalves, H.; Schellenberg, P.; Almeida, B.G. Intense optical second harmonic generation from centrosymmetric nanocrystalline para-nitroaniline. *Appl Phys Lett* **2014**, *104*, 181903.
151. Gonçalves, H.; Saavedra, I.; Ferreira, R.A.; Lopes, P.; de Matos Gomes, E.; Belsley, M. Efficient second harmonic generation by para-nitroaniline embedded in electro-spun polymeric nanofibres. *Journal of Physics D: Applied Physics* **2018**, *51*, 105106.
152. Kolev, T.; Koleva, B.B.; Spiteller, M.; Mayer-Figge, H.; Sheldrick, W.S. 2-Amino-4-nitroaniline, a Known Compound with Unexpected Properties. *The Journal of Physical Chemistry A* **2007**, *111*, 10084-10089.
153. Baptista, R.M.F.; Bernardo, C.R.; Belsley, M.S.; de Matos Gomes, E. Electrospun fibers with highly polarized second harmonic light from 2-amino-4-nitroaniline and 3-nitroaniline nanocrystals embedded in poly-L-lactic acid polymer. *Opt Mater* **2021**, *116*, 111089.
154. Liu, Y.; Pellerin, C. Stability and phase behavior of the poly(ethylene oxide)–urea complexes prepared by electrospinning. *Polymer* **2009**, *50*, 2601-2607.
155. Liu, Y.; Antaya, H.; Pellerin, C. Characterization of the stable and metastable poly(ethylene oxide)–urea complexes in electrospun fibers. *Journal of Polymer Science Part B: Polymer Physics* **2008**, *46*, 1903-1913.
156. Tadokoro, H.; Yoshihara, T.; Chatani, Y.; Murahashi, S. A preliminary report of structural studies on polyethylene oxide-urea complex. *Journal of Polymer Science Part B: Polymer Letters* **1964**, *2*, 363-368.
157. Liu, Y.; Pellerin, C. Highly Oriented Electrospun Fibers of Self-Assembled Inclusion Complexes of Poly(ethylene oxide) and Urea. *Macromolecules* **2006**, *39*, 8886-8888.